



**Lehrstuhl für
Technische Dynamik**
Prof. Dr.-Ing. habil. Sigrid Leyendecker

Report

Chair of Applied Dynamics

2015



**FRIEDRICH-ALEXANDER
UNIVERSITÄT
ERLANGEN-NÜRNBERG**

TECHNISCHE FAKULTÄT

© 2015

Prof. Dr.-Ing. habil. S. Leyendecker

Lehrstuhl für Technische Dynamik

Universität Erlangen-Nürnberg

Haberstrasse 1

91058 Erlangen

Tel.: 09131 8561000

Fax.: 09131 8561011

www: <http://www.ltd.tf.uni-erlangen.de>

Editor: N. Kondratieva

All rights reserved. Without explicit permission of the authors it is not allowed to copy this publication or parts of it, neither by photocopy nor in electronic media.

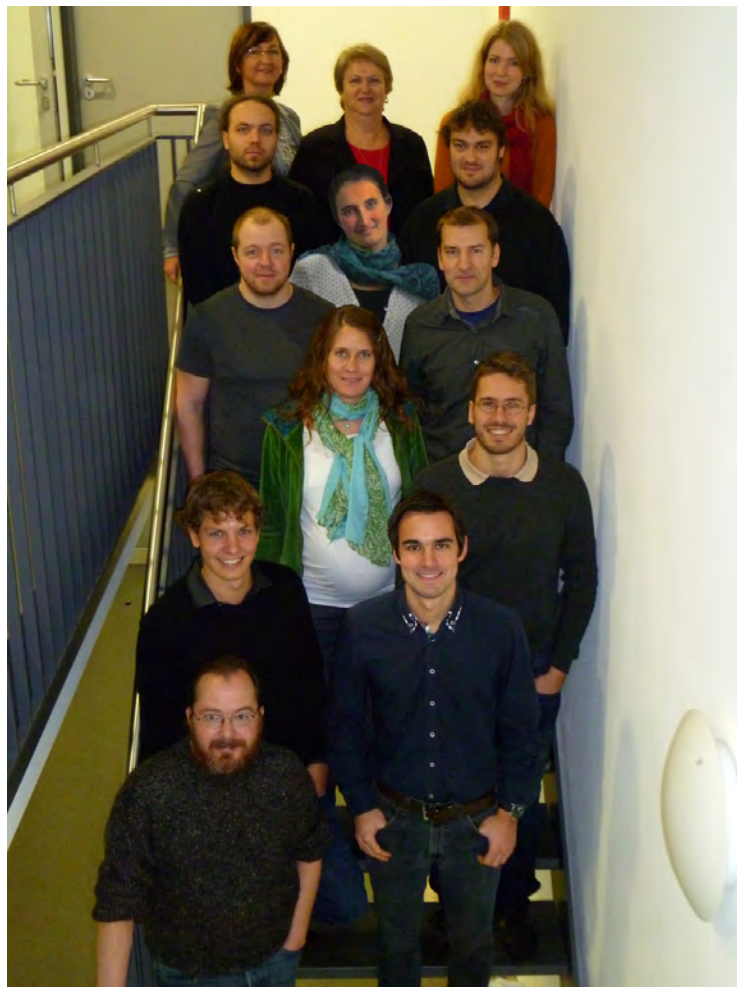
Contents

1	Preface	4
2	Team	5
3	Research	7
3.1	Emmy Noether Independent Junior Research Group	7
3.2	Bionicum	7
3.3	BaCaTeC	7
3.4	GAMM and GACM	7
3.5	Cooperation partners	7
3.6	Scientific reports	8
4	Activities	37
4.1	Teaching	37
4.2	Dynamical laboratory – modeling, simulation and experiment	39
4.3	Theses	41
4.4	Seminar for mechanics	42
4.5	Editorial activities	44
4.6	Long night of science	45
5	Publications	51
5.1	Reviewed journal publications	51
5.2	Reviewed proceeding publications	51
5.3	Talks	51
6	Social events	53

1 Preface

This report summarises the activities in research and teaching of the Chair of Applied Dynamics at the University of Erlangen-Nuremberg between January and December 2015. Part of LTD is the Independent Junior Research Group in the DFG Emmy Noether Programme ‘Simulation and optimal control of the dynamics of multibody systems in biomechanics and robotics’ that has been at the University of Kaiserslautern from May 2009 to March 2011.

The main direction of research is computational dynamics and optimal control. Efficient technologies for dynamical and optimal control simulations are developed, facing contemporary life science and engineering problems. The problems under investigation come from biomechanics (natural or impaired human movements and athletic’s high performance) and robot dynamics (industrial, spatial and medical) as well as the optimisation and optimal control of their dynamics. Further topics are the modelling and simulation of biological and artificial muscles (as electromechanically coupled problems), multiscale and multirate systems with dynamics on various time scales (examples in astrodynamics as well as on atomistic level), higher order variational integrators, Lie group methods and viscous beam formulations as well as research on structural rigidity and conformational analysis of macromolecules. The development of numerical methods is likewise important as the modelling of the nonlinear systems, whereby the formulation of variational principles plays an important role on the levels of dynamic modeling, optimal control as well as numerical approximation, yielding a holistic approach.



2 Team

chair holder

Prof. Dr.-Ing. habil. Sigrid Leyendecker

technical staff

Beate Hegen

Dipl.-Ing. (FH) Natalia Kondratieva

Sven Lässig

academic scientist

Dr. rer. nat. Holger Lang

postdoc

Dr. Odysseas T. Kosmas

until 31.03.2015

Dr.-Ing. Ramona Hoffmann

since 01.08.2015

scientific staff

M.Sc. Dominik Budday

M.Sc. Daniel Glaas

since 01.04.2015

Dipl.-Ing. Tobias Gail

Dipl.-Ing. Thomas Leitz

Dipl.-Math. Maik Ringkamp

Dipl.-Ing. Tristan Schlögl

M.Sc. Theresa Wenger

since 01.04.2015

students

Dominik Bartels

Tim Bassing

Larissa Bugert

Lewin Buttazzo

Emre Cicek

David Elz

Roman Enser

Sebastian Falk

Christian Feuerer

Michele Gleser

Habuer Guerloss

Johannes Henneberg

Alexander Hetzner

Johanna Hilsen

Michael Jäger

Dominik Kalb

Johannes Koch

Julius Kohnert

Johann Penner

Roland Purucker

Dominik Reichl

Uta Rösel

Judith Saffer

Sebastian Scheiterer

Selina Scherzer

Marie-Louise Schlichting

Christian Seifert

Canet Serin

Artur Usbek

Thomas Will

Pascal Zobel

Student assistants are mainly active as tutors for young students in basic and advanced lectures at the Bachelor and Master level. Their indispensable contribution to high quality teaching at the is invaluable, thus financial support from various funding sources is gratefully acknowledged.



B. Hegen



N. Kondratieva



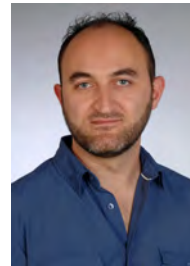
S. Lässig



H. Lang



R. Hoffmann



O.T. Kosmas



D. Budday



T. Gail



D. Glaas



T. Leitz



M. Ringkamp



T. Schlögl



T. Wenger



S. Leyendecker

3 Research

3.1 Emmy Noether Independent Junior Research Group

The Emmy Noether Programme by the German Research Foundation (DFG) supports young researchers in achieving independence at an early stage of their scientific careers. Between May 2009 and March 2011, the Emmy Noether Independent Junior Research Group ‘Simulation and optimal control of the dynamics of multibody systems in biomechanics and robotics’ has been affiliated with the University of Kaiserslautern. The group has been transferred to the University of Erlangen-Nuremberg in April 2011 being now part of the Chair of Applied Dynamics.

3.2 Bionicum

The Bavarian Environment Agency (LfU) (being the central authority for environmental protection and nature conservation, geology and water resources management) has established the centre for bionics ‘bionicum’ in 2012, consisting of a visitors centre in the Tiergarten of the City of Nuremberg with a permanent exhibition and three research projects with a total financial volume of eight million Euro. One of the projects investigates artificial muscles. The modelling and simulation of the dielectric elastomer actors is developed at the LTD while the Institute for Factory Automation and Production Systems (FAPS) works on the fabrication.

3.3 BaCaTeC

The Bavaria California Technology Center at the University of Erlangen-Nuremberg supports newly initiated cooperations between researchers from Bavaria and California. Between July 2014 and December 2015, BaCaTeC sponsored the LTD for the established collaboration with the Stanford Synchrotron Radiation Lightsource (SSRL) on ‘Inferring rigid substructures in proteins from X-ray data using the null space topology’. The project ended successfully, with two scientific publications this year in the Journal of the Mechanics and Physics of Solids and the Proceedings in Applied Mathematics and Mechanics.

3.4 GAMM and GACM

Sigrid Leyendecker has been elected as an Executive Council Member of the German Association for Computational Mechanics (GACM) for the period of January 2013 to December 2016. The objective of GACM is to stimulate and promote education, research and practice in computational mechanics and computational methods in applied sciences, to foster the interchange of ideas among various fields contributing to computational mechanics, and to provide forums and meetings for the dissemination of knowledge about computational mechanics in Germany.

In February 2014, she has further been elected as a member of the Managing Board of the International Association of Applied Mathematics and Mechanics (GAMM) for two years. GAMM promotes scientific development in all areas of applied mathematics and mechanics, e.g. via the organisation of workshops, in particular for younger scientists, and the international scientific annual GAMM meeting.

3.5 Cooperation partners

Besides numerous worldwide cooperations with scientists in academia, the LTD is in contact with other institutions and industrial partners. The LTD cooperates with the Fraunhofer Institute for Industrial and Economical Mathematics (ITWM) in Kaiserslautern on common interests like biomechanics and nonlinear rod dynamics for wind turbine rotor blades. A cooperation with the AG wearHEALTH and AG Augmented Vision, Department Computer Science, TU Kaiserslautern and German Research

Center for Artificial Intelligence (DFKI), aims at bridging the gap between motion capturing and biomechanical optimal control simulations. In collaboration with the Stanford Synchrotron Radiation Lightsource (SSRL), the LTD does research on structural rigidity and conformational analysis of biomolecules.

3.6 Scientific reports

The following pages present a short overview on ongoing research projects pursued at the Chair of Applied Dynamics. These are partly financed by third-party funding (German Research Foundation (DFG), Bavarian Environment Agency (LfU)) and in addition by the core support of the university.

Research topics

Complex frequency response for linear beams with Kelvin-Voigt viscoelastic material

Holger Lang, Sigrid Leyendecker

Modelling protein conformational transitions with clash- and constraint-guided motion planning

Dominik Budday, Sigrid Leyendecker, Henry van den Bedem

Numerical convergence study for variational multi rate integrators

Tobias Gail, Sina Ober-Blöbaum, Sigrid Leyendecker

Optimal feedback control for constrained mechanical systems

Daniel Glaas, Sigrid Leyendecker

Towards bridging the gap between motion capturing and biomechanical optimal control simulations

Ramona Hoffmann, Tobias Gail, Bertram Taetz, Markus Miezal, Gabriele Bleser, Sigrid Leyendecker

Multisymplectic variational integrators for PDEs of geometrically exact beam dynamics using algorithmic differentiation

Thomas Leitz, Sigrid Leyendecker

Time transformed mixed integer optimal control problems with impacts

Maik Ringkamp, Sina Ober-Blöbaum, Sigrid Leyendecker

Dielectric elastomer actuated multibody systems

Tristan Schlögl, Sigrid Leyendecker

Construction and analysis of higher order variational integrators for dynamical systems with holonomic constraints

Theresa Wenger, Sina Ober-Blöbaum, Sigrid Leyendecker

Complex frequency response for linear beams with Kelvin-Voigt viscoelastic material

Holger Lang, Sigrid Leyendecker

We inspect the complex frequency response for linear homogeneous and uniform beams with Kelvin-Voigt viscoelastic material [2, 4]. The dynamic motion of such a beam is described by the real displacement function $u(x, t)$ satisfying the partial differential equation

$$\rho A \frac{\partial^2 u}{\partial t^2} = \frac{\partial}{\partial x} \left(EA \frac{\partial u}{\partial x} + \eta A \frac{\partial^2 u}{\partial t \partial x} \right) + n \quad \text{where } 0 \leq x \leq L \quad 0 \leq t < \infty \quad (1)$$

denote the undeformed arclength parameter of the centreline and the time, respectively. Further, $L > 0$ is the total length of the beam and $A > 0$ is its cross section area. Thereby, $E > 0$ denotes the extensional (i.e. Young's) modulus, $\eta \geq 0$ the extensional viscosity of the material [3, 4], where $\rho > 0$ is the mass volume density. The function $n = n(x, t)$ is a prescribed exterior axial force line density acting along the rod. For $\eta = 0$, the well-known equation of motion for a purely elastic (i.e. Hookean) axial beam is rediscovered [1, 5]. We rescale the involved magnitudes in (1) according to

$$U(\xi, \tau) = \frac{1}{L} u(x, t) \quad \xi = \frac{x}{L} \quad \tau = \frac{\sqrt{E}}{L\sqrt{\rho}} t \quad \zeta = \frac{\eta}{2L\sqrt{\rho E}} \quad N = \frac{n}{EA}$$

Then, equation (1) becomes free of any physical dimension and reads

$$\ddot{U} = U'' + 2\zeta \dot{U}'' + N \quad \text{where } 0 \leq \xi \leq 1 \quad 0 \leq \tau < \infty \quad (2)$$

Here $\dot{(\cdot)} = \partial(\cdot)/\partial\tau$ and $(\cdot)' = \partial(\cdot)/\partial\xi$. The only remaining independent model parameter is the viscosity $\zeta \geq 0$.

As an example, we consider the 'cantilever' or 'clamped-free' problem with boundary conditions $U(0, \tau) = U'(1, \tau) \equiv 0$. We assume that $N(\xi, \tau) \equiv 0$. It is straightforward to see that real eigen-solutions of (2) take the form

$$U_k(\xi, \tau) = e^{-\Omega_k^2 \zeta \tau} \sin(\Omega_k \xi) \begin{cases} A_k \cos(\Omega_k \sqrt{1 - \Omega_k^2 \zeta^2} \tau) + B_k \sin(\Omega_k \sqrt{1 - \Omega_k^2 \zeta^2} \tau) & \text{if } \zeta < \zeta_k^* \\ A_k + B_k \tau & \text{if } \zeta = \zeta_k^* \\ A_k \exp(\Omega_k \sqrt{\Omega_k^2 \zeta^2 - 1} \tau) + B_k \exp(-\Omega_k \sqrt{\Omega_k^2 \zeta^2 - 1} \tau) & \text{if } \zeta > \zeta_k^* \end{cases} \quad (3)$$

for $k = 0, 1, 2, \dots$. Here, the numbers

$$\Omega_k = \left(k + \frac{1}{2}\right)\pi \quad \text{resp.} \quad \zeta_k^* = \frac{1}{\Omega_k} \quad (4)$$

denote the k -th natural undamped eigenfrequency of the beam resp. the critical viscosity of the k -th eigenmode as defined in [2]. Note that by construction, they do not carry any physical dimension. Note that – coincidentally – Ω_k represents the k -th wave number of the beam [1, 5]. We define the total critical viscosity by

$$\zeta^* = \zeta_0^*.$$

For the boundary conditions under consideration, we have $\zeta^* = 2/\pi$.

The plots in Figures 1 and 2 display the displacement $U(1, \tau)$ and the strain $U'(0, \tau)$ of the transient analytic displacement solution $U(\xi, \tau)$ of (2) under the initial conditions $U(\xi, 0) = \xi$, $\dot{U}(\xi, 0) \equiv 0$ in the case of free vibrations. $U(\xi, \tau)$ can be expressed as linear superposition of the contributions in (3) with appropriate integration constants A_k and B_k , uniquely determined by the initial conditions. The contribution $U_k(\xi, \tau)$ is oscillatory for each k satisfying $\zeta < \zeta_k^*$, but purely viscous for each k satisfying $\zeta \geq \zeta_k^*$.

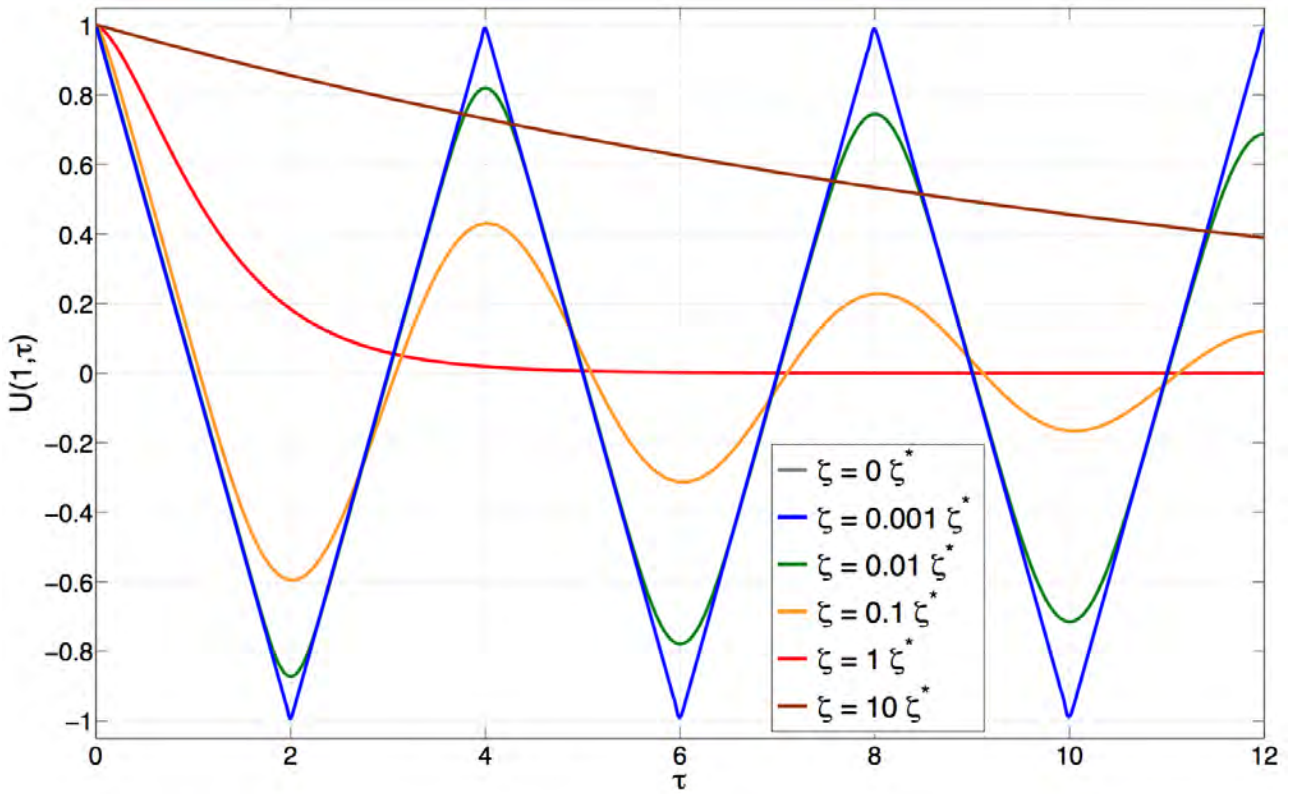


Figure 1: Transient displacement solution $U(1, \tau)$ for free vibrations in the time domain

- For $\zeta = 0$ (grey), the first undamped eigenfrequency is given by $\Omega_0 = \pi/2$. This corresponds to the oscillating period of precisely $2\pi/\Omega_0 = 4$ in τ -time.
- Slight damping for $\zeta = 0.01\zeta^*$ (green), corresponding to $\zeta = 0.01\zeta_0^* = 0.03\zeta_1^* = 0.05\zeta_2^* = \dots$, or even $\zeta = 0.1\zeta^*$ (orange), corresponding to $\zeta = 0.1\zeta_0^* = 0.3\zeta_1^* = 0.5\zeta_2^* = \dots$, damps out all higher frequent contributions.
- For $\zeta = \zeta^*$ (red), mode 0 is damped out critically. Modes 1, 2, ... are overdamped.
- For even larger damping, $\zeta > \zeta^*$ (brown), there is purely viscous creep.

The plot in Figure 3 displays the real amplitude (i.e. norm) $\|U_\Omega(1)\|$ of the complex frequency response function $U_\Omega(\xi)$ at $\xi = 1$, the function $U(\xi, \tau) = U_\Omega(\xi)e^{i\Omega\tau}$ being the node displacement response under exterior forced harmonic excitation $U'(1, \tau) = e^{i\Omega\tau}$ at the rod's free right end $\xi = 1$ under clamped boundary conditions $U(0, \tau) \equiv 0$ at the rod's left end $\xi = 0$.

- For $\zeta = 0$ (grey), each $\Omega = \Omega_k$ according to (4) produces a pole (yielding a resonance catastrophe). Arbitrary high frequencies may be excited, cf. [1, 5].
- Very slight damping $\zeta = 0.001\zeta^*$ (blue) regularises these singularities, as expected. Thus, resonances become finite.
- Slight damping, e.g. for $\zeta = 0.01\zeta^*$ (green) resp. $\zeta = 0.1\zeta^*$ (orange), damps out all vibrations with frequencies larger than Ω_6 resp. Ω_1 . The lowest peak at $\Omega \lesssim \Omega_0 = \pi/2$ contributes to the well recognisable smallest frequency in the transient solutions on the left.

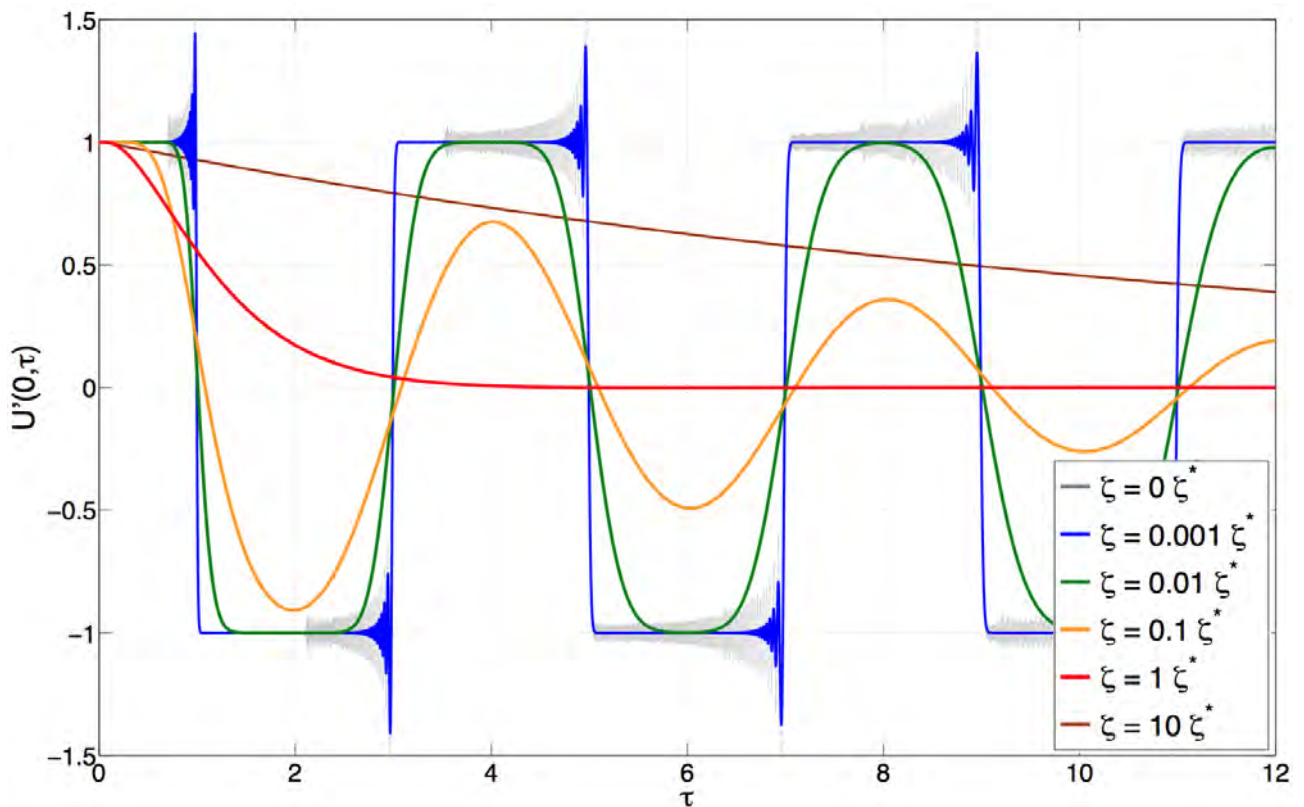


Figure 2: Transient strain solution $U'(0, \tau)$ for free vibrations in the time domain

- For $\zeta \geq \zeta^*$, no vibrations are possible any more. ($\zeta = \zeta^*$ is in fact the smallest viscosity for which all oscillations are absorbed.)

Independent of the value of ζ , each amplitude curve $\|U_\Omega(1)\|$ converges to unity for $\Omega = 0$, which comprises the important special case of statics. At $\Omega = 0$, the function $\|U_\Omega(1)\|$ possesses vanishing slope, if $\zeta \leq \zeta^*$.

The results in Figures 2 and 3 are obtained numerically by the use of the finite element method with a sufficiently large number of 400 linear elements [6]. After semi-discretisation, the transient analytical solutions, depicted at the left, are gained by the time integration methods ODE45 (for $\zeta = 0$) and ODE15S (for $\zeta > 0$) in MATLAB [7]. It can be shown that in the context of finite dimensional linear dynamic structures [1, 5], Kelvin-Voigt viscoelasticity for linear beams leads to structural damping, if the material and geometry data are homogeneously distributed.

Further discussion, analytical aspects and the treatment of linear torsional and bending beams of Euler-Bernoulli kind with Kelvin-Voigt material are part of further investigation and research.

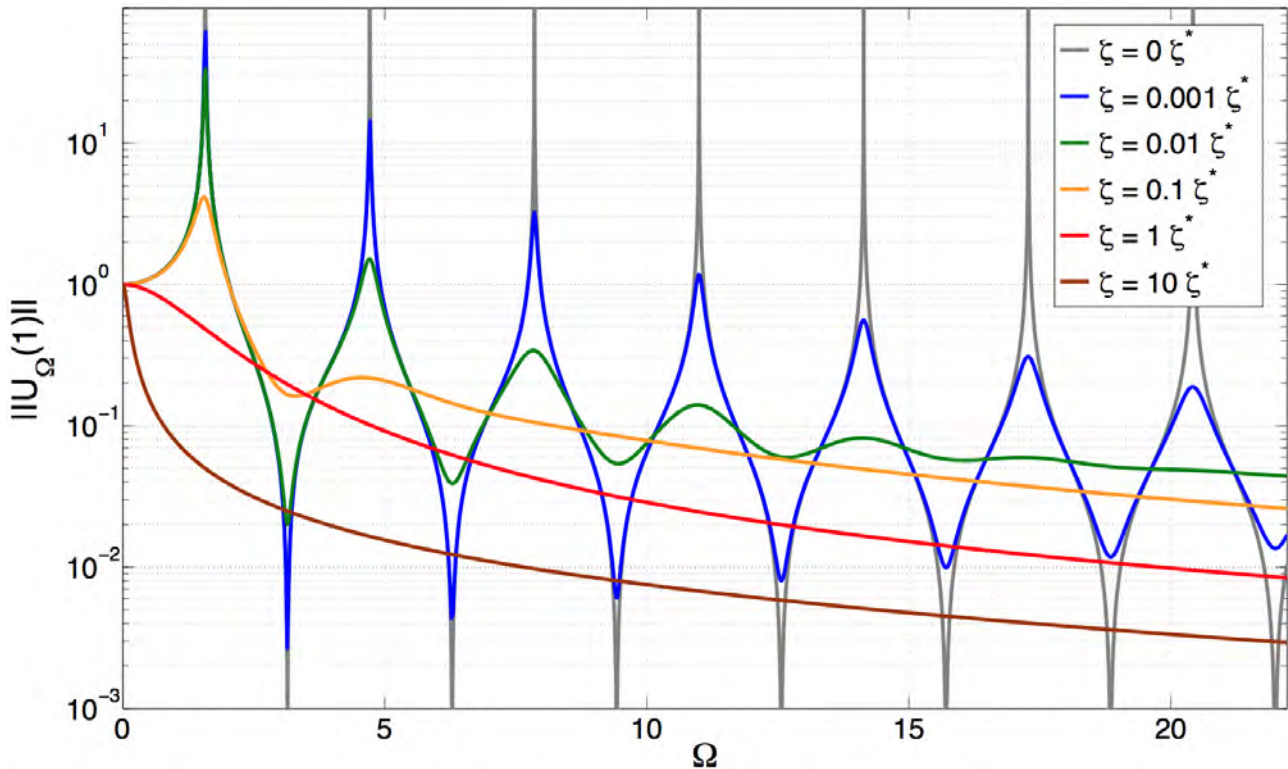


Figure 3: Amplitude solution $\|U_{\Omega}(1)\|$ for harmonic forced excitation in the frequency domain

References

- [1] R. R. Craig and A. J. Kurdila, *Fundamentals of structural mechanics*. Wiley, 2006.
- [2] H. Lang, S. Leyendecker, and J. Linn, “Numerical experiments for viscoelastic Cosserat rods with Kelvin-Voigt damping”, in *Proceedings of the ECCOMAS Thematic Conference on Multibody Dynamics*, July 1-4, Zagreb, Croatia, 2013.
- [3] J. Lemaitre and J. L. Chaboche, *Mechanics of solid materials*. Cambridge university press, 1998.
- [4] J. Linn, H. Lang, and A. Tuganov, “Geometrically exact Cosserat rods with Kelvin-Voigt type viscous damping”, *Mechanical Sciences*, Vol. 4, pp. 79-96, 2013.
- [5] L. Meirovitch, *Fundamentals of vibrations*. McGraw-Hill, 2001.
- [6] H. R. Schwarz, *Finite element methods*. Teubner, 1991.
- [7] L. F. Shampine and M. W. Reichelt. *The Matlab ODE suite*. SIAM journal on scientific computing, Vol. 18, No. 1, pp. 1-22, 1997.

Modelling protein conformational transitions with clash- and constraint-guided motion planning

Dominik Budday, Sigrid Leyendecker, Henry van den Bedem

Proteins exist as interconverting conformational ensembles, exchanging between substates to perform their function. Advances in experimental techniques give us unprecedented access to structural snapshots of their conformational landscape. However, computationally modeling how proteins use collective motions to transition between substates is challenging owing to conflictive objectives: distance minimization, clash prevention, and maintaining a folded, authentic state. We developed a robotics-inspired motion planning procedure to connect two substates that overcomes the rugged landscape by introducing dynamic, interatomic constraints. This algorithm is based on our molecular framework [1, 2] that describes proteins as kinematic linkages. We enforce clash-preventing, holonomic constraints for pairs of atoms whenever their distance falls below a predefined threshold, which balances clashes and flexibility.

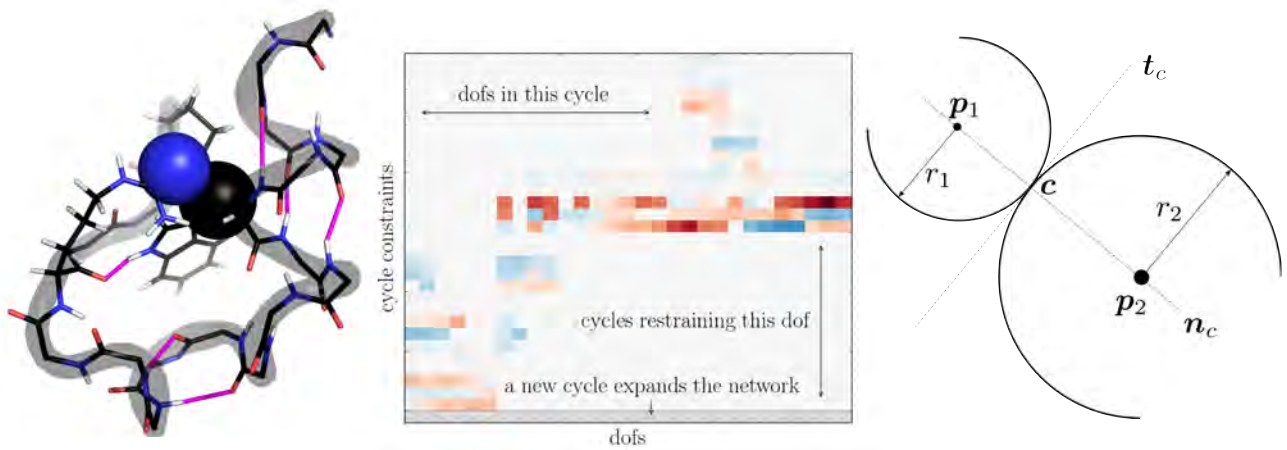


Figure 1: A protein's flexibility is highly constrained by hydrogen bonds (shown in pink) and steric clashes (shown as spheres) (left). The constraint Jacobian matrix reveals in a column which cycles restrain a degree of freedom and in a row which degrees of freedom are part of an individual cycle. This nesting of cycles propagates collective motion. A new cycle, i.e. an additional row, expands the network (middle). Geometry of two clashing atoms at contact (right)

Our molecular framework represents proteins as kinematic spanning trees, with groups of atoms as rigid body vertices and covalent, rotatable bonds as links or edges with a torsional degree of freedom [1, 2]. Non-covalent hydrogen bonds are encoded as pentavalent holonomic constraints $\Phi(\mathbf{q}) = \mathbf{0} \in \mathbb{R}^{5m}$ that only allow a rotation about their bond axis, which lead to m nested, interdependent cycles that require coordinated changes of the d torsional angles $\mathbf{q} \in \mathbb{R}^d$ in the molecule. Admissible velocities $\dot{\mathbf{q}}$ lie in the nullspace of the constraint Jacobian matrix \mathbf{J} , i.e. $\mathbf{J}\dot{\mathbf{q}} = \mathbf{0}$. The nullspace basis \mathbf{N} relates independent velocities $\dot{\mathbf{u}}$ to admissible velocities via $\dot{\mathbf{q}} = \mathbf{N}\dot{\mathbf{u}}$, which allows us to identify rigidified dihedral angles and hydrogen bonds [1, 2]. In this spirit, a nullspace projection $\Delta_{\mathbf{q}} = \mathbf{N}\mathbf{N}^T\delta_{\mathbf{q}}$ of a trial vector $\delta_{\mathbf{q}}$ provides access to efficiently sample conformation space while maintaining constraints in linear approximation. Using a seed conformation, we obtain a new sample via $\mathbf{q}_{new} = \mathbf{q}_{seed} + \Delta_{\mathbf{q}}$. To account for multi-chain proteins and complexes, we link the spanning trees of individual chains by an additional covalent bond taken from the set of inter-chain hydrogen bonds. In addition to hydrogen bonds, clashes restrain a protein's flexibility (Figure 1 (left)). Figure 1 (right) shows the contact conformation of two atoms centered at \mathbf{p}_1 and \mathbf{p}_2 . The unit normal vector at contact is $\mathbf{n}_c = \frac{\mathbf{p}_2 - \mathbf{p}_1}{|\mathbf{p}_2 - \mathbf{p}_1|}$,

tangent vectors are denoted by \mathbf{t}_c . We define the clash distance \bar{d} as the sum of their van der Waals radii $\bar{d} = c_f(r_1 + r_2)$, with a scaling parameter c_f . If a small perturbation Δ_q results in a conformation with $|\mathbf{p}_2 - \mathbf{p}_1| < \bar{d}$, the sample is discarded and, instead, a new constraint

$$\mathbf{n}_c^T \left(\frac{\partial \mathbf{p}_2}{\partial \mathbf{q}} - \frac{\partial \mathbf{p}_1}{\partial \mathbf{q}} \right) \dot{\mathbf{q}} = 0 \quad (1)$$

is formed. This equality constraint maintains the distance along \mathbf{n}_c and only allows a joint move in \mathbf{n}_c direction, or individual moves in \mathbf{t}_c direction, letting the atoms slide past each other. A basis for the new nullspace is given by $\mathbf{N}_{cp} \in \mathbb{R}^{d \times (d-r')}$, with r' the rank of the resulting Jacobian.

We incorporate a bidirectional rapidly exploring random tree [3] to identify possible transition pathways in proteins. This motion planning strategy simultaneously expands a forward and a reverse tree from the initial conformation \mathbf{q}_{init} and target conformation \mathbf{q}_{target} to find a connecting path. We integrate our Dynamic Clash Avoiding Constraint (DyCAC) strategy to iterate along clash boundaries to overcome barriers in conformation space and identify new, clash-free conformations.

We generate an entirely random conformation and expand the forward tree towards the random conformation using the node \mathbf{q}_{seed} closest in heavy-atom RMSD in the tree. To direct the search towards the final conformation, we introduce a bias at which an actual target is selected at random from the opposing tree with a frequency of 60%. An admissible velocity is obtained by calculating a mean squared distance (MSD) gradient δ_q with respect to atom positions towards the target and projecting the gradient. If a trial move δ_q leads to a clash-free sample \mathbf{q}_{new} , we append a new node and edge to the forward tree. Following the 'CONNECT' strategy [3], we use the new sample as seed for the next iteration and proceed further to the same target. If δ_q leads to clashes, we add constraints (1) to the clashing atoms. We re-apply δ_q a specified number of times, using the clash-free projection equation $\mathbf{N}_{cp} \mathbf{N}_{cp}^T \delta_q$, until a clash-free sample is obtained. The new constraints are released at this stage. If our search is unable to advance, i.e. we cannot find a new clash-free sample, we swap trees and propagate in the other direction. After the swap, a new target conformation and the closest existing node on the forward tree are computed. The procedure ends when the distance between the trees falls below a threshold or when we reach a specified number of samples. We restart the algorithm every 1000 samples using the two closest nodes in heavy-atom RMSD on the forward and reverse tree.

If δ_q leads to clashes, we add constraints (1) to the clashing atoms. We re-apply δ_q a specified number of times, using the clash-free projection equation $\mathbf{N}_{cp} \mathbf{N}_{cp}^T \delta_q$, until a clash-free sample is obtained. If our search is unable to advance, i.e. we cannot find a new clash-free sample, we swap trees and propagate in the other direction. The procedure ends when the distance between the trees falls below a threshold or when we reach a specified number of samples. We restart the algorithm every 1000 samples using the two closest nodes in heavy-atom root mean square distance (RMSD) on the forward and reverse tree.

Figure 2 (left) shows the evolution of the fractional RMSD between the two propagating trees. In six out of seven cases, the RMSD could be significantly reduced. Figure 2 (right) shows the forward and reverse tree for the first 1000 samples of protein Gas, with color representing reduced mobility due to additional clash constraints. Figure 3 finally shows the initial (left), target (mid-left) and final aligned conformations of the forward and reverse tree (mid-right). We observe great agreement in the RAS and the α -helical domain. The right panel shows the cumulative change of torsion angles during the forward transition.

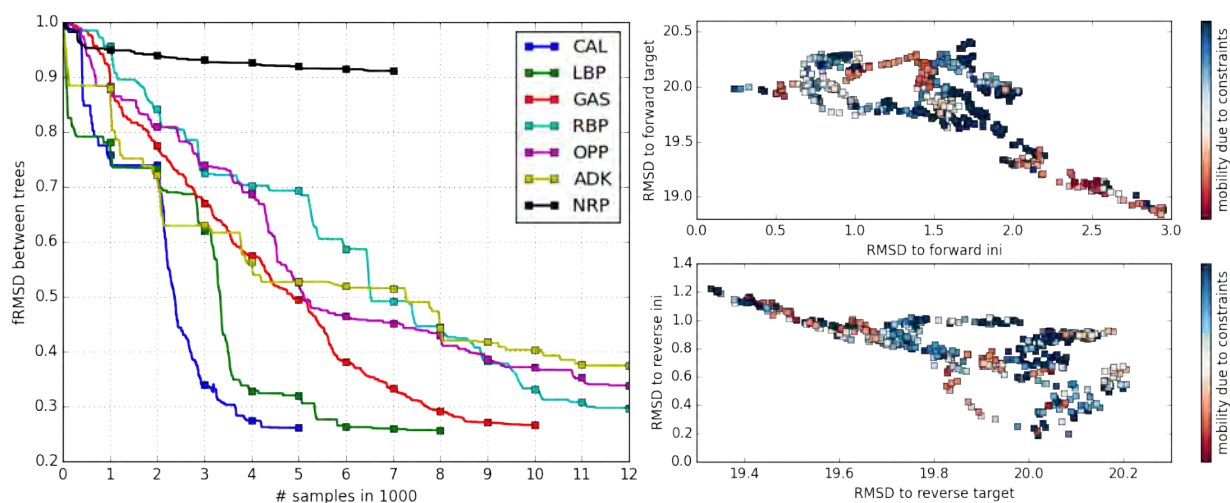


Figure 2: Evolution of RMSD (heavy atoms) between the two propagating trees during exploration of the test proteins. We iteratively restart the RRT after 1000 samples (left). Forward and reverse tree for the first 1000 samples of protein *Gas*. Color represents mobility at an individual conformation due to additional clash constraints, with blue encoding no clash constraint (right).

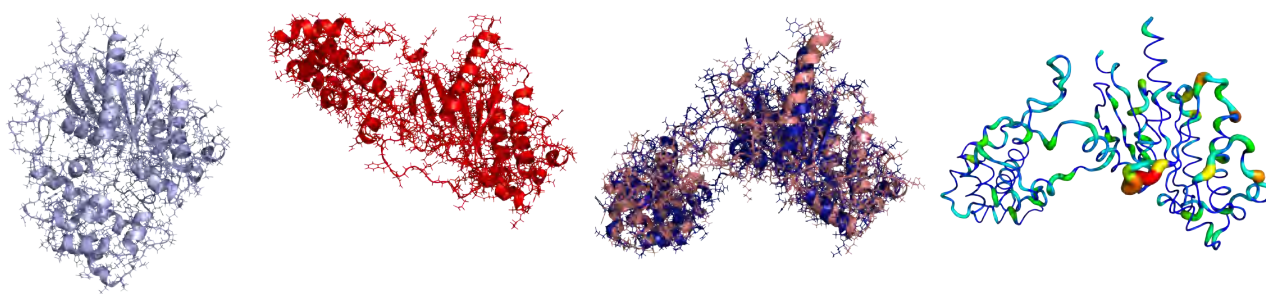


Figure 3: Conformational transition of *Gas* with initial, inactive conformation (left), active target conformation (mid-left) and superimposed final conformations of the forward (dark blue) and reverse (salmon) tree. The RMSD is 5.32\AA (mid-right). Cumulative change of torsion angles between the initial and the final conformation of the forward tree. Thicker and red-shifted backbone areas contribute more to conformational changes (right).

References

- [1] D. Budday, S. Leyendecker, H. van den Bedem. *Geometric analysis characterizes molecular rigidity in generic and non-generic protein configurations*. Journal of the Mechanics and Physics of Solids, Vol. 83, pp. 36–47, 2015.
- [2] D. Budday, S. Leyendecker, H. van den Bedem. *A geometric approach to characterize rigidity in proteins*. Proc. Appl. Math. Mech., Vol. 15 (1), pp. 89–90, 2015.
- [3] J. Kuffner, S. Lavalle. *RRT-connect: An efficient approach to single-query path planning*. Robotics and Automation, ICRA'00 IEEE International Conference, 2000.

Numerical convergence study for variational multirate integrators

Tobias Gail, Sina Ober-Blöbaum, Sigrid Leyendecker

The integration of a mechanical system containing slow and fast dynamics has contradicting requirements. On the one hand, for a stable integration of the fast dynamics, tiny time steps are needed. On the other hand, for the slow dynamics, larger time steps are accurate enough. Furthermore, too small time steps increase the computing time unnecessarily, especially for costly function evaluations.

For this, multirate formulations split the system into subsystems [1] which can be solved with different methods. To approximate the solution, rather than choosing one time grid we choose two time grids. Figure 3 shows such a time grid with macro time grid and micro time grid. Here, the macro time step is ΔT , the micro time step is Δt and $\Delta T \geq \Delta t$ holds. As described in the framework of variational multirate integration [2] which is developed on the basis of variational integrators. This approach leads to a reduction of computing time, see [3]. The numerical convergence is investigated for unconstrained systems like the Fermi-Pasta-Ulam problem (FPU) illustrated in Figure 2 and systems subject to constraints like the simple atomic model (SAM) shown in Figure 1.

Let a mechanical system be described by a Lagrangian with configuration vector $q(t) \in Q \subseteq \mathbb{R}^n$ with Q a configuration manifold and velocity vector $\dot{q} \in TQ \subseteq \mathbb{R}^n$ in the tangent space TQ . Also, let the mechanical system be constrained by the m^c -dimensional holonomic function of constraints requiring $g(q) = 0$. Now, let the mechanical system contain slow and fast dynamics, characterised by the possibility to split the variables into n^s slow variables q^s and n^f fast variables q^f with $q = (q^s, q^f)$ and $n = n^s + n^f$. Furthermore, we assume that we can split the potential energy into a slow potential $V(q)$ and a fast potential $W(q^f)$. The action S is the time integral of the Lagrangian $L(q, \dot{q}) = T(\dot{q}) - V(q) - W(q^f)$. Via Hamilton's principle requiring stationarity of the action $\delta S = 0$, the constrained multirate Euler-Lagrange equations are derived. Here, T denotes the kinetic energy and λ the Lagrange multiplier.

$$\begin{aligned} \frac{d}{dt} \frac{\partial T}{\partial \dot{q}^s} - \frac{\partial V}{\partial q^s} - \left(\frac{\partial g}{\partial q^s} \right)^T \cdot \lambda &= 0 \\ \frac{d}{dt} \frac{\partial T}{\partial \dot{q}^f} - \frac{\partial V}{\partial q^f} - \frac{\partial W}{\partial q^f} - \left(\frac{\partial g}{\partial q^f} \right)^T \cdot \lambda &= 0 \\ g(q) &= 0 \end{aligned} \tag{1}$$

The macro time grid provides the domain for the discrete slow variables $q_d^s = \{q_k^s\}_{k=0}^N$ with $q_k^s \approx q^s(t_k)$, while the micro time grid provides the domain for the discrete fast variables $q_d^f = \{\{q_k^{f,m}\}_{m=0}^p\}_{k=0}^{N-1}$

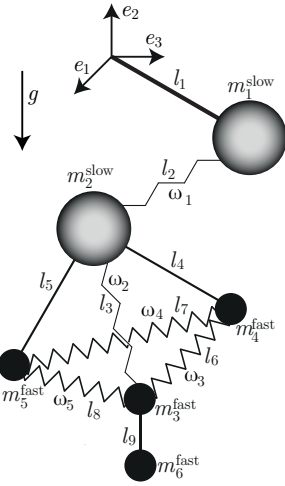


Figure 1: SAM with slow and fast variables



Figure 2: FPU with 6 masses and slow and fast variables

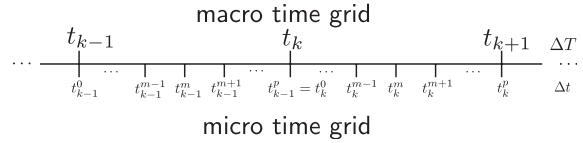


Figure 3: Macro and micro time grid

with $q_k^{f,m} \approx q^f(t_k^m)$. The domain for the discrete Lagrange multipliers is the macro and the micro grid, for example on the micro time grid $\lambda_d = \{\{\lambda_k^m\}_{m=0}^p\}_{k=0}^{N-1}$ with $\lambda_k^m \approx \lambda(t_k^m)$. The discrete Lagrangian and the discrete constraints approximate the action over one macro time step.

$$L_d(q_k^s, q_{k+1}^s, q_k^f, \lambda_k) \approx \int_{t_k}^{t_{k+1}} L(q, \dot{q}) - g(q)^T \cdot \lambda dt.$$

The sum over all time steps is the discrete action which approximates the continuous action. Via a discrete form of Hamilton's principle requiring stationarity for the discrete action, we derive the discrete constrained multirate Euler-Lagrange equations. These equations form a nonlinear set of equations which are solved using a Newton-Raphson method.

Quadrature rules are needed to approximate the action and constraints by discrete quantities. We use e.g. the midpoint rule, the trapezoidal rule, an affine combination and finite difference. Different quadrature rules can be chosen for the kinetic energy, both potential energies and the constraints and lead to "fully implicit", "explicit slow, implicit fast" and "fully explicit" schemes.

The convergence is shown numerically for the FPU and the SAM example for the fully implicit, explicit slow, implicit fast and the fully explicit quadrature schemes. The global error

$$e_q = \sup_{k=0, \dots, N} \{\|q_k - q(t_k)\|\} \tag{2}$$

of the configuration as well as the error e_p of the conjugate momentum is calculated for all quadrature schemes at the macro nodes. Both global errors are plotted versus the macro time steps ΔT for the FPU and for the SAM in Figure 4. We see on the left hand side convergence of order two for both systems for the fully implicit scheme. On the right hand side, a convergence of order one is shown for the fully explicit scheme. In the middle, there is a difference in order of convergence for the two systems. The top left shows a convergence of order one for the FPU and the bottom plot shows a convergence of order 1.5 for the SAM.

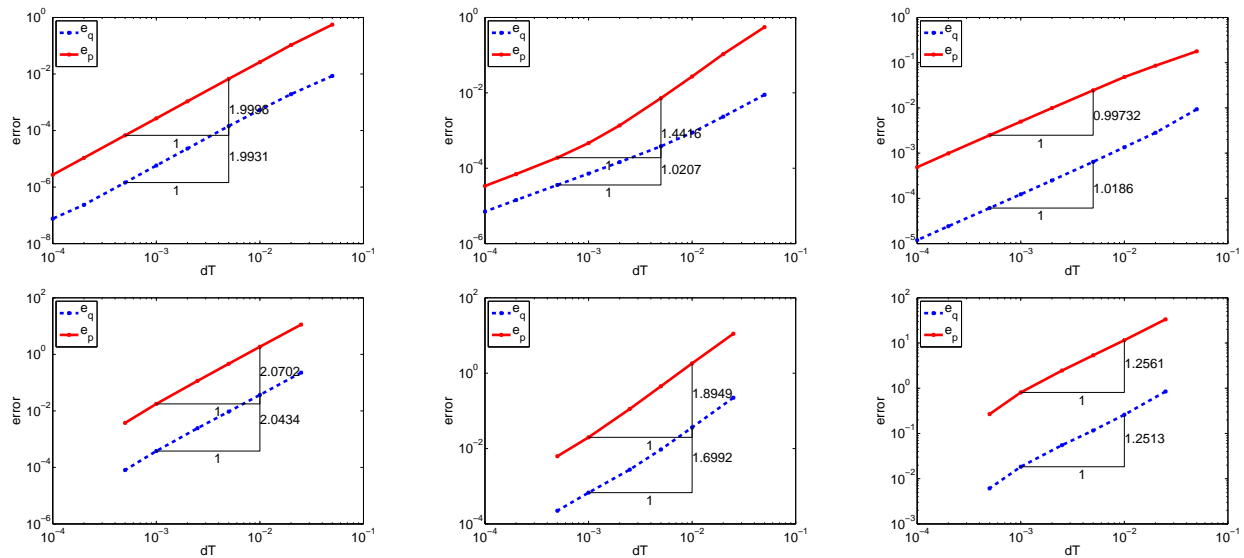


Figure 4: Error of configuration and conjugate momentum with $p = 5$ and $\Delta T \rightarrow 0$, $\Delta t \rightarrow 0$ for the fully implicit scheme (left), explicit slow, implicit fast (middle) and fully explicit (right) for FPU (top) and SAM (bottom)

References

- [1] M. Arnold. *Multi-rate time integration for large scale multibody system models*. IUTAM Symposium on Multiscale Problems in Multibody System Contacts, P. Eberhard (ed), Vol. 195(50-51), pp. 1-10, Springer, 2007.
- [2] S. Leyendecker, and S. Ober-Blöbaum. *A Variational approach to multirate integration for constrained systems*. Multibody Dynamics, Computational Methods in Applied Sciences, Computational Methods in Applied Sciences, J. C. Samin, P. Fiset (eds.), pp. 97-121, Springer, 2013.
- [3] T. Gail, S. Leyendecker, and S. Ober-Blöbaum. *Computing time investigations of variational multirate integrators*. Proceedings of the Multibody Dynamics ECCOMAS Thematic conference, Zagreb, Croatia, pp. 603-612, 1-4 July 2013.
- [4] A. Stern, and E. Grinspun. *Implicit-explicit variational integration of highly oscillatory problems*. Multiscale Model. Simul., Vol. 7(4), pp. 1779-1794, 2009.

Optimal feedback control for constrained mechanical systems

Daniel Glaas, Sigrid Leyendecker

Today, a lot of mechanical systems have to operate with an improved performance compared to equal constructions decades ago. Reasons therefore are e.g. higher energy costs and a globalised market with more competitors. To stay competitive, engineers of a mechanical systems need to find an optimal control algorithm.

Variational integrator and DMOC The variational integrator as a variant of a structure-preserving integration scheme is used. The continuous Lagrange function $L(q, \dot{q}) = T(q, \dot{q}) - V(q)$ and the

action integral $S(q) = \int_0^T L(q, \dot{q}) dt$ yield the Euler-Lagrange equations via a variational principle [2]. Using a midpoint quadrature rule to approximate the action integral and applying a discrete variational principle $\delta S_d(\{q_k\}_{k=0}^{N_t}) = 0$ with configuration sequence $q_k \approx q(t_k)$ for $k = 0, \dots, N_t$ and an approximation of the virtual work with control sequence $\{u_k\}_{k=0}^{N_t-1}$, the Lagrange-d'Alembert principle yields a discrete Euler-Lagrange equation in a "position-momentum form that only depends on the current and future time steps" [1]. This principle is applied to three different coordinate choices, at first in minimal coordinates with $q_k \in \mathbb{R}^f$, $p_k \in \mathbb{R}^f$, in redundant coordinates with $q_k \in \mathbb{R}^n$, $p_k \in \mathbb{R}^n$ by using holonomic constraints $g(q(t)) = 0 \in \mathbb{R}^m$, $G(q_k) = \frac{\partial g(q_k)}{\partial q_k}$ and the nullspace coordinates with $q_k \in \mathbb{R}^n$, $p_k \in \mathbb{R}^f$ using the nullspace matrix $P^T(q_k) \cdot G^T(q_k) = 0 \in \mathbb{R}^{f \times (n-f)}$. The equations for the redundant coordinates in "pq-formulation" are

$$\begin{aligned} p_k + \frac{\partial L_d(q_k, q_{k+1})}{\partial q_k} + F_d^-(q_k, q_{k+1}, u_k) - G^T(q_k) \lambda_k \Delta t &= 0 \\ g(q_{k+1}) &= 0 \\ p_{k+1} &= \frac{\partial L_d(q_k, q_{k+1})}{\partial q_{k+1}} + F_d^+(q_k, q_{k+1}, u_k) \end{aligned}$$

Together with initial and final conditions for the configuration and conjugate momentum, the discrete equations serve as non-linear equality constraints for the minimisation of a given objective functional. Applying the DMOC (discrete mechanics and optimal control, see [4, p. 49-52]) algorithm, an optimal trajectory and according control input is calculated.

Riccati-controller Even when knowing an optimal trajectory $x_{opt} = [q_{opt} \ p_{opt}]^T$ of a system, in reality the mechanical system will not follow the predefined path because of several perturbations. The correction of these are done by feedback controllers. The main idea of the control mechanism is

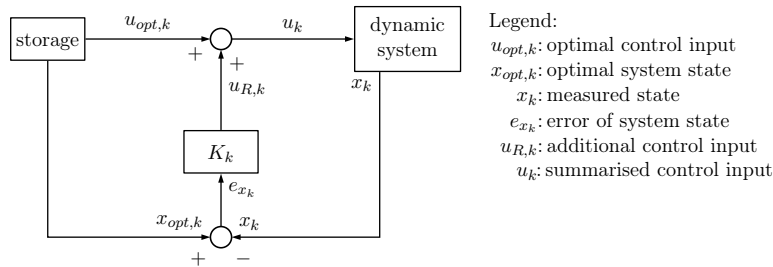


Figure 1: Block diagram of general feedback control

to add an additional value u_R to the optimal control input $u_k = u_{opt,k} + u_{R,k}$ based on the superposition principle. In general, u_R is defined as a function of e_x for the time step k , i.e. $u_{R,k} = f(e_{x_k})$, with e_{x_k} being the difference between the desired state space x_{opt} and the "measured" state space x , i.e. $e_{x_k} = x_{opt,k} - x_k$. Often, a linear feedback multiplication with the feedback matrix K_k

$$u_{R,k} = f(e_{x_k}) = K_k e_{x_k} \quad (1)$$

does fine. The resulting block structure is shown in Figure 1. In the background of the optimal control approach, the Riccati feedback controller is commonly used to minimise a cost-function $V = \sum_{k=0}^{N_t-1} [e_{x_k}^T Q_k e_{x_k} + u_{R,k}^T R_k u_{R,k}] + e_{x_{N_t}}^T Q_{N_t} e_{x_{N_t}}$ with real weighting matrices Q_k and R_k . After linearising the system to $\delta x_{k+1} = A_k \cdot \delta x_k + B_k \cdot \delta u_k$, the discrete Riccati equation (see [3, Eq. (14.5), (14.6)])

can be applied

$$P_k = Q_k + A_k^T P_k A_k - A_k P_k B_k^T [R_k + B_k^T P_k B_k]^{-1} B_k^T P_k A_k \quad (2)$$

$$K_k = [R_k + B_k^T P_k B_k]^{-1} B_k^T P_k A_k \quad (3)$$

Using symmetric positive definite matrices for Q_k and R_k , P_k can be implicitly calculated as positive defined solution of (2) (see [3, p. 298]). After that, the matrix K_k as defined in (3) and the optimal additional control input u_R is calculated. Figure 2 shows the complete process of the optimal control in

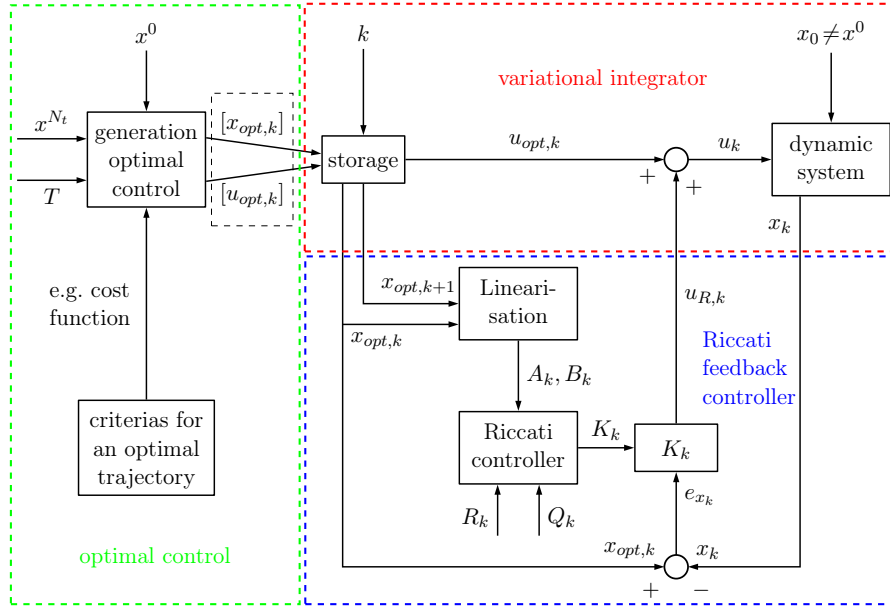


Figure 2: Block diagram of feedback control for optimal trajectories with the Riccati approach

a block diagram, beginning with the preprocessing of generating an optimal trajectory (green dashed box). These results are the input for the variational integrator (red dashed box), which simulates the behaviour of the real physical system and is extended by the Riccati feedback controller (blue dashed box) to calculate $u_{R,k}$.

2D-pendulum The described algorithm is applied to the 2D-pendulum as shown in Figure 3. The configuration, momentum and actuation vectors are defined as

- minimal: $q_{\min} = \theta$, $p_{\min} = p_\theta$, $u_{\min} = u$
- redundant: $q_{\text{red}} = [x \ y]^T$, $p_{\text{red}} = [p_x \ p_y]^T$,
 $u_{\text{red}} = [F_x \ F_y]^T$
- nullspace: $q_{\text{null}} = [x \ y]^T$, $p_{\text{null}} = p_\theta$, $u_{\text{null}} = [F_x \ F_y]^T$.

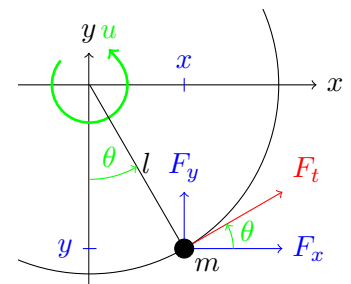


Figure 3: Parametrisation of the 2D-pendulum

For comparing the Riccati-control algorithm for the three parametrisations, an optimal upswing from $\theta^0 = 0$ to $\theta^{N_t} = \pi$ is calculated in DMOC. For disturbed initial conditions $\theta_0 = 1$, the corrected trajectories of all three implementations are very similar compared to each other as plotted in Figure 4. Only during the time of 0.1s to 0.7s, there are some slight differences.

Based on this the control effort is compared, being the sum of all past time steps over a term weighting

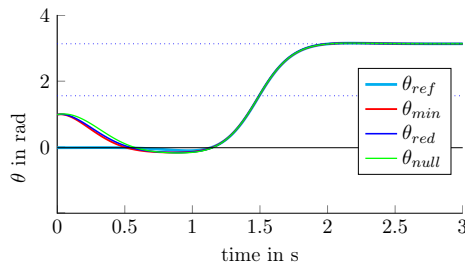


Figure 4: Comparison of the configuration trajectory of variational integrator with feedback controller for all coordinate choices for $T=3\text{s}$ and $\Delta t=0.01\text{s}$

the effort of the additional control $V_{u_k} = \sum_{i=0}^k u_{R,i}^T R u_{R,i}$. In Figure 5, V_{u_k} is plotted for all three coordinate choices.

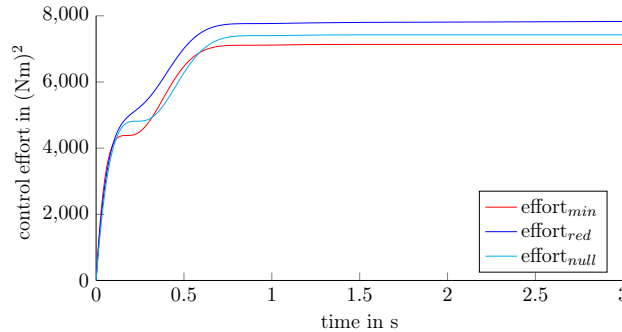


Figure 5: Comparison of the control effort of variational integrator with feedback controller for all coordinate choices for $T=3\text{s}$ and $\Delta t=0.01\text{s}$

All graphs are strictly increasing as being a sum of positive terms and the gradient corresponds to the difference of the controlled trajectory to the reference trajectory. After the first second, all three sums are changing only very slightly. Comparing the absolute values, the minimal coordinates scheme requires least control effort with the best accuracy whereas the redundant coordinates scheme has the highest control effort. The nullspace parametrisation is situated in the middle between the other two.

References

- [1] E. Johnson, J.A. Schultz, and Todd D Murphey. Structured linearization of discrete mechanical systems for analysis and optimal control. *IEEE Transactions on Automation Science and Engineering*, 12:140–152, 2015.
- [2] S. Leyendecker, J.E. Marsden, and M. Ortiz. Variational integrators for constrained dynamical systems. *ZAMM - Journal of Applied Mathematics and Mechanics / Zeitschrift für Angewandte Mathematik und Mechanik*, 88(9):677–708, 2008.
- [3] J. Lunze. *Regelungstechnik 2: Mehrgrößensysteme, digitale Regelung; 8., überarb. Aufl.* Springer-Lehrbuch. Springer Vieweg, Berlin [u.a.], 2014.
- [4] S. Ober-Blöbaum, O. Junge, and J. E. Marsden. Discrete mechanics and optimal control: An analysis. *ESAIM: COCV*, 17(2):322–352, 2011.

Towards bridging the gap between motion capturing and biomechanical optimal control simulations

Ramona Hoffmann, Tobias Gail, Bertram Taetz, Markus Miezal, Gabriele Bleser, Sigrid Leyendecker

Within this work, we make a first attempt towards improving human motion capture by combining motion capturing measurements and optimal control simulations of a human steering motion. We start with measurements obtained from a stationary optical system, a widespread capturing technology in biomechanics and movement science, under laboratory conditions. From an optimal control point of view, the goal is to increase the realism of simulated human motion through measurements. From a motion capturing point of view, the goal is to compensate for measurement sparsity, errors or lacks through meaningful assumptions based on biomechanical simulation. Our preliminary results show that a fusion of physical laws, biomechanical simulation and real data within an optimal control simulation framework indeed have the potential to improve motion capture and synthesis with respect to some of their inherent problems.

Human arm model For the simulation, the human arm is modelled as a multibody system consisting of three rigid bodies. A cylindrical upper arm is fixed in space by a spherical joint representing the shoulder. The elbow and wrist are modelled as cardan joints connecting the cylindrical forearm to the upper arm and the parallelepiped shaped hand to the forearm, respectively (see Figure 1). The bodies' dimensions are personalised for the subject and the optical marker positions are placed manually in the model based on measurements. Thus, the exact definition of the personalised model is already a result from the measured data.

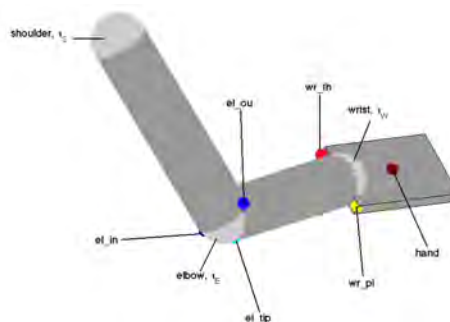


Figure 1: Human arm model with marker positions used for optimal control simulations. The three markers around the elbow are denoted $el.in$, $el.out$, $el.tip$. The two markers at the wrist are denoted $wr.th$ and $wr.pi$. There is one marker on the hand.

Optimal control problem and simulation Two inherently different approaches for the solution of an optimal control problem are the so called indirect (first optimise then discretise) and direct (first discretise then optimise) approach, see e.g., [7, 2]. In this work, a direct transcription method called discrete mechanics and optimal control for constrained systems (DMOCC), see [4, 6], falling into the latter class, is used to approximate the solution at the time nodes $t_0, t_1 = t_0 + h, \dots, t_N = t_0 + Nh$ on an equidistant time grid with time step h . As described in detail in [1], the kinematic description of the rigid multibody system is based on a redundant configuration variable $q_k \in \mathbb{R}^{36}, k = 0, \dots, N$ consisting of the placement of the centre of mass and the orientation represented by three directors that are aligned with the principal axes of inertia for each rigid body, respectively. A set of 29 holonomic constraints ensure orthonormality of each body's directors (thus they represent the columns of a rotation matrix) as well as the coupling by the joints, thus the complete model has 7 degrees of freedom.

A nodal reparametrisation $F_d : \mathbb{R}^7 \rightarrow \mathbb{R}^{36}$ updates the redundant configuration $q_{k+1} = F_d(u_{k+1}, q_k)$ for $k = 0, \dots, N-1$ in terms of discrete generalised coordinates $u_d = \{u_k\}_{k=1}^N$ with $u_k \in \mathbb{R}^7$ such that the constraints are fulfilled. In contrast to a formulation in terms of minimal coordinates (joint angles) from the beginning, this procedure ensures that rotations are always small and thus avoids the danger of singularities. The configuration variable q can be treated in a linear space, yielding a Lagrangian function with a constant mass matrix. A structure preserving scheme (symplectic-momentum with good energy behaviour) approximates the dynamics. It is derived via a discrete variational principle, see [5], where a discrete Lagrangian $L_d : \mathbb{R}^{36} \times \mathbb{R}^{36} \rightarrow \mathbb{R}$ approximates the action in one time interval. The discrete Euler-Lagrange equations resulting from the stationary condition for the discrete action are reduced to minimal dimension using a discrete null space matrix $P(q_k) \in \mathbb{R}^{36 \times 7}$ and the nodal reparametrisation F_d resulting in (2), see [1, 3]. They involve the left and right control forces $f_{k-1}^+ = B(q_k) \cdot \tau_{k-1}$, $f_k^- = B(q_k) \cdot \tau_k \in \mathbb{R}^{36}$ which are computed from the discrete generalised controls $\tau_d = \{\tau_k\}_{k=0}^{N-1}$ with joint torques $\tau_k \in \mathbb{R}^7$ (assumed to be constant during one time interval) using the input transformation matrix $B(q_k) \in \mathbb{R}^{7 \times 36}$, see [4] for a detailed introduction to DMOCC. The optimal control problem is simulated solving the following nonlinear constrained optimisation problem using an SQP algorithm in Matlab. Minimisation of the objective function J_d

$$\min_{u_d, \tau_d} J_d(u_d, \tau_d) \quad (1)$$

subject to the fulfilment of the discrete equations of motion

$$P^T(q_k) \cdot [D_2 L_d(q_{k-1}, q_k) + D_1 L_d(q_k, F(u_{k+1}, q_k)) + f_{k-1}^+ + f_k^-] = 0 \quad (2)$$

boundary conditions

$$s(u_d, \tau_d) = 0 \quad (3)$$

and path constraints

$$h(u_d, \tau_d) \leq 0 \quad (4)$$

We perform optimal control simulations with different objective functions and path constraints. The measured marker positions are part of the inequality constraints. First a feasible trajectory is generated, after that physiologically motivated cost functions are used:

- Feasible trajectory. State and control trajectories that are feasible in the sense that they fulfil the equations of motion (2) and boundary conditions (3) are obtained by minimising the objective

$$J_d(u_d, \tau_d) = 1$$

with the additional path constraints (4) imposing an upper bound $\epsilon \in \mathbb{R}$ on the marker position's residual errors taking the form

$$h(u_d, \tau_d) = \sum_{k=0}^N (m_k - \bar{m}_k)^T \cdot (m_k - \bar{m}_k) - \epsilon \quad (5)$$

- Minimisation of torque. The second cost function minimises the control effort

$$J_d(u_d, \tau_d) = \frac{\Delta t}{2} \sum_{k=0}^{N-1} \tau_k^T \cdot \tau_k$$

subject to the discrete equations of motion (2), boundary conditions (3) and path constraints (5).

- Minimisation of torque change. In the last problem, the temporal torque change is minimised, thus

$$J_d(u_d, \tau_d) = \frac{\Delta t}{2} \sum_{k=0}^{N-2} \left\| \frac{\tau_{k+1} - \tau_k}{\Delta t} \right\|^2$$

while the discrete equations of motion (2), boundary conditions (3) and path constraints (5) are fulfilled.

Results Reducing the measurement update rate results in a range between 100 and 7.69 Hz. Figures 2 and 3 show the error statistics for the tested measurement rates based on a piecewise constant and a piecewise linear initial guess, respectively. Error is here defined as the Euclidean distance between the configurations q obtained from the reference simulation (using a measurement frequency of 100 Hz in the feasible, torque minimising and torque change minimising simulation) and the simulation with reduced measurement update rate at each time node $t_k, k = 0, \dots, N$. The figures then report the average error and its standard deviation for a complete simulation (y -axis) over the measurement rate (x -axis). Each vertical line (illustrating the standard deviation) represents one successful simulation. Missing vertical lines indicate a simulation failure, e.g., due to divergence of the SQP algorithm. Note that errors are computed only in the time interval $[0, 0.39]$ s, since \bar{m}_{39} is the last measurement used in all simulations.

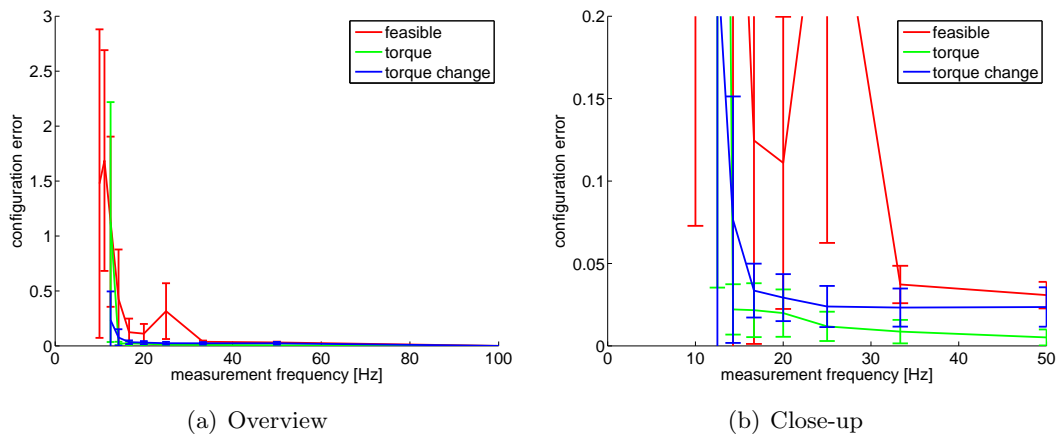


Figure 2: Mean errors and standard deviations based on piecewise constant initial guess.

When comparing Figures 2 and 3, in particular the close-ups, it can be observed that some simulation experiments have failed below 20 Hz when using a piecewise constant initialisation. Hence, linear interpolation enables convergence at very low measurement update rates. Moreover, it can be seen in the figures that linear interpolation also reduces the overall errors. This is particularly visible for the feasible solution.

When looking at Figure 3, as expected, the errors and standard deviations increase with reduced measurement update rate for all solutions. However, the error of the feasible solution is consistently higher than the error of the solutions including a physiological cost function term. Below 20 Hz, errors and standard deviations of the feasible solution increase significantly and the last two simulations even fail. In contrast, minimising torque and torque change show a better behaviour. Minimal torque shows the lowest error until 12.5 Hz, however, then starts to increase significantly, and fails for the last simulation at 7.69 Hz. Minimal torque change successfully converges for all experiments and shows a comparably small error increase even at the lowest measurement frequencies. These observations confirm that, in our experimental settings, biomechanical simulation can compensate for low measurement update rates. Moreover, while the torque minimising solution provides the most

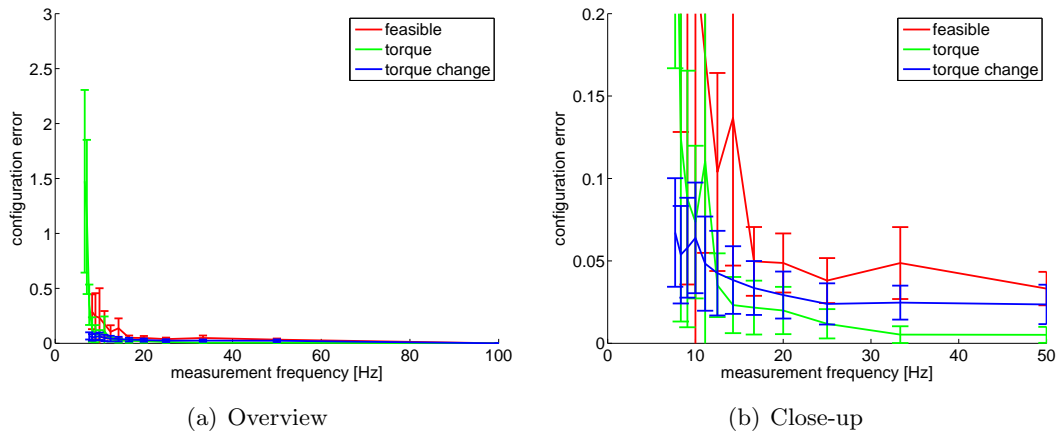


Figure 3: Mean errors and standard deviations based on piecewise linear interpolation for initial guess.

accurate results down to a certain measurement rate, the torque change minimising solution provides acceptable accuracy for even lower measurement update rates, hence adds further stability. To provide more detailed insights, Figure 4 illustrates the error evolution in q (configuration error) for two concrete measurement update rates (using linear interpolation for the initial guess). We chose 33.3 Hz (every 3rd measurement) as representative for a mid-range frequency and 8.33 Hz (every 12th measurement) as lowest frequency with results for all solutions.

These figures confirm the above observations. In addition, it is nicely visible in Figure 4(b), that the errors show a periodic pattern induced by the measurement update rate, i.e., the error becomes lower around measurement points. This is most apparent for the feasible solution, but also clearly visible for the minimal torque solution. Interestingly, the minimal torque change solution, even if showing a slightly higher error than the minimal torque solution for the mid-range frequency, is much less affected by the measurement points. This might indicate a higher independence from measurements, a better ability to deal with errors in these and, as a result, a higher robustness. On the other hand, also error of the time stepping equations (with respect to an analytical solution) grows as the simulation advances in time. This point needs further investigation in the future. One can also observe that the error tends to decrease throughout the simulation, in particular for the low measurement update rate and the minimal torque and torque change solutions.

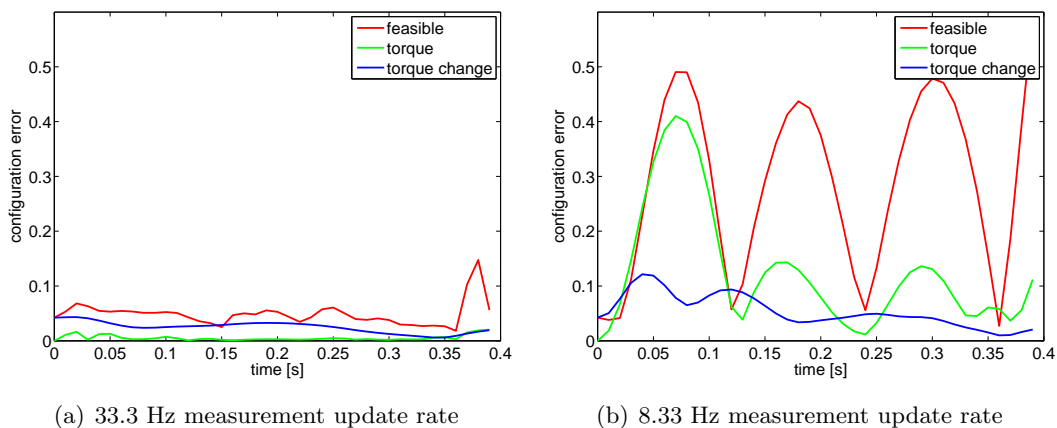


Figure 4: Error evolution in configuration q .

From the investigated objective functions here, minimising torque change shows the most realistic and natural results and the highest stability with respect to the reduction of the measurement frequency. The most obvious future task is to confirm these observations with different types of motions and other physiologically motivated objective functions. Furthermore, it is worthwhile to take into account also measurements of the bodies orientation instead of only marker point positions and information on the accelerations and angular velocities measured from inertial sensors. In particular, the latter means not merely the inclusion of more and different type of data, but the move towards ambulatory motion capturing may overcome many of the shortcomings of optical stationary systems discussed in the introduction and enable a wide range of applications outside the lab. However, also many technical aspects need to be investigated. If there is knowledge on the precession or error-proneness of certain measurements, weighting factors can be introduced accordingly. Secondly, not only the measurement rate, but also the number of marker positions can be reduced, excluding ,e.g., those with most soft tissue artefacts.

Finally, the inclusion of further information known about the considered motion, like the presence of obstacles in the environment or contact to the surroundings, as, e.g., of the hand moving on a circle due to its contact to the steering wheel, may help to increase the realism and naturalness of the simulated motion.

References

- [1] P. Betsch and S. Leyendecker. *The discrete null space method for the energy consistent integration of constrained mechanical systems. Part II: Multibody dynamics* Int. J. Numer. Meth. Engng., Vol. 67(4), pp. 499-552, 2006.
- [2] J. Betts. *Survey of numerical methods for trajectory optimization*. Journal of Guidance, Control, and Dynamics, Vol. 21(2), pp. 193-207, 1998.
- [3] S. Leyendecker, J. Marsden, and M. Ortiz. *Variational integrators for constrained dynamical systems*. ZAMM, Vol. 88(9), pp. 677-708, 2008.
- [4] S. Leyendecker, S. Ober-Blöbaum, J. Marsden, and M. Ortiz. *Discrete mechanics and optimal control for constrained systems*. Optimal Control Applications & Methods, Vol. 31(6), pp. 505-528, 2010. DOI: 10.1002/oca.912.
- [5] J. Marsden and M. West. *Discrete mechanics and variational integrators*. Acta Numerica, Vol. 10, pp. 357-514, 2001.
- [6] S. Ober-Blöbaum, O. Junge, and J. Marsden. *Discrete mechanics and optimal control: an analysis*. ESAIM: Control Optimisation and Calculus of Variations, Vol. 17(2), pp. 322-352, 2010. DOI: 10.1051/cocv/2010012.
- [7] O. von Stryk and R. Bulirsch. *Direct and indirect methods for trajectory optimization*. Annals of Operations Research, pp. 357-373, 1992.

Multisymplectic variational integrators for PDEs of geometrically exact beam dynamics using algorithmic differentiation

Thomas Leitz, Sigrid Leyendecker

For the simulation of geometrically exact beam dynamics [4], a multisymplectic Lie-group variational integrator [3] is derived. Based on the implementation of the discrete Lagrangian, algorithmic differentiation is used in the computation of both, the discrete Euler-Lagrange equations, and the Jacobi matrix needed for the Newton-Raphson iteration. Using $s, t \in \mathbb{R}$ as arc-length and time parameters, translational degrees of freedom of the cross-sections are parameterized using three-dimensional vectors $x(s, t) \in \mathbb{R}^3$ and rotational degrees of freedom are parameterized using unit-quaternions $p(s, t) \in \mathbb{H}^1$. In geometrically exact beam dynamics, the cross-sections stay plane and undeformed at all times. The Lagrange density for geometrically exact beams $L(p, \omega, \Omega, x, \dot{x}, x', s)$ is given in terms of the translational velocities and strains $\dot{x} = \frac{d}{dt}x$ and $x' = \frac{d}{ds}x$ and rotational velocities and strains $\omega = 2\bar{p}\dot{p}$ and $\Omega = 2\bar{p}p'$. Hamilton's principle leads to the continuous Euler-Lagrange equations in the form of partial differential equations. The discrete Lagrangian L_a^j is an approximation of the action integral of an

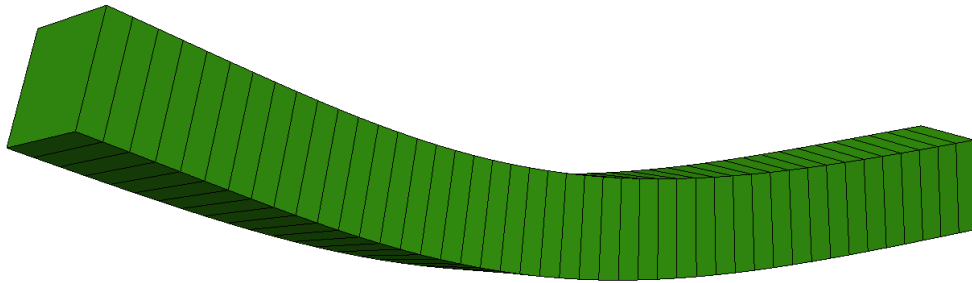


Figure 1: A beam with 44 elements

element in a regular spacetime grid and the discrete action S_d is the sum over all discrete Lagrangians covering spacetime. Each spacetime element has four nodes, a is the space index and j is the time index, thus we write $p_a^j = p(t^j, s_a)$. Positions are interpolated bilinearly and for the rotations, we use quaternion linear blending (QLB) and subsequent differentiation with respect to s and t in order to derive discrete velocities and strains. With $\alpha_i = \frac{t-t^j}{t^{j+1}-t^j}$ and $\beta^i = \frac{s-s_a}{s_{a+1}-s_a}$, P_a^j is the interpolation

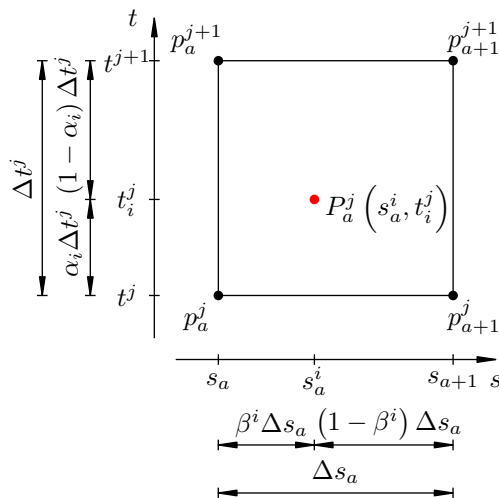


Figure 2: Spacetime element for the interpolation between the four corners

between the four nodes of one spacetime element (see Figure 2)

$$P_a^j(s, t) = \frac{(1 - \beta^i) \left((1 - \alpha_i) p_a^j + \alpha_i p_a^j \right) + \beta^i \left((1 - \alpha_i) p_{a+1}^j + \alpha_i p_{a+1}^j \right)}{\left\| (1 - \beta^i) \left((1 - \alpha_i) p_a^j + \alpha_i p_a^j \right) + \beta^i \left((1 - \alpha_i) p_{a+1}^j + \alpha_i p_{a+1}^j \right) \right\|}$$

and the discrete angular velocity and strain are

$$\begin{aligned} \omega_a^j(s, t) &= 2\bar{P}_a^j \dot{P}_a^j = \frac{1}{B^2} \frac{2}{\Delta t^j} \left[(1 - \beta^i)^2 \mathfrak{S}(\bar{p}_a^j p_a^{j+1}) + (\beta^i)^2 \mathfrak{S}(\bar{p}_{a+1}^j p_{a+1}^{j+1}) \right. \\ &\quad \left. + (1 - \beta^i) \beta^i \left(\mathfrak{S}(\bar{p}_a^j p_{a+1}^{j+1}) + \mathfrak{S}(\bar{p}_{a+1}^j p_a^{j+1}) \right) \right] \\ \Omega_a^j(s, t) &= 2\bar{P}_a^j P_a^j = \frac{1}{B^2} \frac{2}{\Delta s_a} \left[(1 - \alpha_i)^2 \mathfrak{S}(\bar{p}_a^j p_a^j) + (\alpha_i)^2 \mathfrak{S}(\bar{p}_{a+1}^{j+1} p_{a+1}^{j+1}) \right. \\ &\quad \left. + (1 - \alpha_i) \alpha_i \left(\mathfrak{S}(\bar{p}_a^j p_{a+1}^{j+1}) + \mathfrak{S}(\bar{p}_{a+1}^{j+1} p_a^j) \right) \right] \end{aligned}$$

According to the discrete Hamilton's principle, the variation of the discrete action vanishes, i.e. $\delta S_d = 0$, while holding the boundaries of spacetime fixed. This leads to the coupled mixed frame discrete Euler-Lagrange equations

$$\begin{bmatrix} \frac{1}{2} \mathfrak{S} \left(\bar{p}_a^j \frac{\partial L_a^j}{\partial p_a^j} + \bar{p}_a^j \frac{\partial L_a^{j-1}}{\partial p_a^j} + \bar{p}_a^j \frac{\partial L_{a-1}^j}{\partial p_a^j} + \bar{p}_a^j \frac{\partial L_{a-1}^{j-1}}{\partial p_a^j} \right) \\ \frac{\partial L_a^j}{\partial x_a^j} + \frac{\partial L_a^{j-1}}{\partial x_a^j} + \frac{\partial L_{a-1}^j}{\partial x_a^j} + \frac{\partial L_{a-1}^{j-1}}{\partial x_a^j} \end{bmatrix} = \begin{bmatrix} 0 \\ 0 \\ 0 \\ 0 \\ 0 \\ 0 \end{bmatrix}$$

These form the variational integrator and are implemented using the C++ algorithmic differentiation library CppAD [1] in conjunction with the linear algebra library Eigen [2]. This object oriented approach leads to rapid development of new integrators through the combination of the expressive syntax of Eigen and the elimination of the need for symbolic derivatives by algorithmic differentiation.

References

- [1] B. M. Bell. *CppAD: a package for C++ algorithmic differentiation*. Computational Infrastructure for Operations Research, 2012.
- [2] G. Guennebaud, B. Jacob, and others. *Eigen v3*. 2010.
- [3] J.E. Marsden, G.W. Patrick, and S. Shkoller. *Multisymplectic geometry, variational integrators, and nonlinear PDEs*. Communications in Mathematical Physics, Vol. 199, pp. 351-395, December 1998.
- [4] J Simo. *A finite strain beam formulation. The three-dimensional dynamic problem. Part I*. Computer Methods in Applied Mechanics and Engineering, Vol. 49(1), pp. 55-70, May 1985.

Time transformed mixed integer optimal control problems with impacts

Maik Ringkamp, Sina Ober-Blöbaum, Sigrid Leyendecker

Mixed integer control systems are used to model dynamical behavior that can change instantly, for example a driving car with different gears [1]. Changing a gear corresponds to an instant change of the differential equation what is achieved in the model by changing the value of the integer control function. The optimal control of a mixed integer control system by a discretize-then-optimize approach leads to a mixed integer nonlinear optimization problem (MINLP) that is not differentiable with respect to the integer variables, such that gradient based optimization methods can not be applied to solve the MINLP at once. In this work, differentiability with respect to all optimization variables is achieved by reformulating the mixed integer optimal control problem (MIOCP) using a time transformation. The time transformed mixed integer optimal control problem (TMIOCP) is shortly introduced, it allows to change the sequence of active differential equations while the discretized problem does not have integer optimization variables. Thus, the discretized TMIOCP is an ordinary nonlinear program (NLP) and gradient based optimization methods can be applied to solve it. In contrast to other works, here MIOCPs where impactive switches are caused due to mechanical contact are taken into account. Forced and constrained Hamiltonian systems with a Hamiltonian $H_l : \mathbb{R}^{n_q} \times \mathbb{R}^{n_p} \rightarrow \mathbb{R}$, holonomic constraints $g_l^h : \mathbb{R}^{n_q} \rightarrow \mathbb{R}^{n_{g^h}}$ and control forces $f_l : \mathbb{R}^{n_q} \times \mathbb{R}^{n_p} \times \mathbb{R}^{n_u} \rightarrow \mathbb{R}^{n_q}$ for each integer value $l \in \mathcal{V} = \{1, 2, \dots, n_{\mathcal{V}}\}$ are investigated. The purely continuous differential algebraic equation for each $l \in \mathcal{V}$ is defined as follows

$$\dot{q} = \frac{\partial H_l}{\partial p}(q, p) \quad (1)$$

$$\dot{p} = f_l(q, p, u) - \frac{\partial H_l}{\partial q}(q, p) - \frac{\partial (g_l^h)^T}{\partial q}(q) \lambda \quad (2)$$

$$0 = g_l^h(q) \quad (3)$$

The functions $q : I \rightarrow \mathbb{R}^{n_q}$ and $p : I \rightarrow \mathbb{R}^{n_p}$ (for a time interval $I = [t_0, t_f]$) represent the position and the momentum of the dynamical system, $\frac{\partial (g_l^h)^T}{\partial q}(q) \lambda$, with time dependent $\lambda(t) \in \mathbb{R}^{n_{g^h}}$ represents the constraint forces. A Hamiltonian is typically given by $H_l(q, p) = T_l(q, p) + V_l(q)$ with the systems kinetic energy $T_l(q, p) = \frac{1}{2} p^T (M_l(q))^{-1} p$ and its potential energy $V_l(q)$. The matrix $M_l(q)$ is symmetric and positive definite and thus invertible. A simple example for a force function is the thrust of an engine, that is directly given by u with $f_l(q(t), p(t), u(t)) = u(t)$. Denoting the right-hand side of (1) and (2) by $F(x, u, l)$ and the state by $x = (q, p)$, leads after the time transformation to the differential equation (5). Further, the holonomic constraints $g_l^h(q) = 0$ can be integrated in the integer dependent mixed state-control constraints $g(x, u, l) \leq 0$ and lead after the time transformation to (7). The constraints $g(x, u, l) \leq 0$ are in general used to restrict x and u to specific domains $D_l = \{(x, u) \in \mathbb{R}^{n_x} \times \mathbb{R}^{n_u} | g(x, u, l) \leq 0\}$ if the integer value $l \in \mathcal{V}$ is active (cf. [2]). Further possible integer independent mixed state-control constraints (6), constraints associated with the time transformation (9), (10) as well as boundary constraints (8) in combination with an objective (4) define the TMIOCP as follows

Definition 1 (TMIOCP)

$$\min_{x,u,w} \quad J^*(x,u,w) = \int_I w(\tau)B(x(\tau),u(\tau),\bar{v}_{N,n}(\tau)) d\tau \quad (4)$$

$$\text{s. t.} \quad \dot{x}(\tau) = w(\tau)F(x(\tau),u(\tau),\bar{v}_{N,n}(\tau)) \quad \text{for a.e. } \tau \in I \quad (5)$$

$$g_0(x(\tau),u(\tau)) \leq 0 \quad \text{for a.e. } \tau \in I \quad (6)$$

$$w(\tau)g(x(\tau),u(\tau),\bar{v}_{N,n}(\tau)) \leq 0 \quad \text{for a.e. } \tau \in I \quad (7)$$

$$r(x(t_0),x(t_N)) = 0 \quad (8)$$

$$w(\tau) \geq 0 \quad \text{for a.e. } \tau \in I \quad (9)$$

$$\Delta I_j = \int_{I_j} w(s)ds \quad (10)$$

Here, $\bar{v}_{N,n} \in \mathcal{L}^\infty(I, \mathcal{V})$ denotes the fixed integer control function and $w \in \mathcal{L}^\infty(I, \mathbb{R})$ the time control, see [2]. The Equation (9) ensures that the transformed time does not move backwards and (10) ensures that major time grid nodes are fixed. It is necessary to fix the major time grid nodes to guarantee a certain accuracy of the approximated trajectories and a fixed total maneuver time. The time transformed differential algebraic equation (1)-(3) is discretized for each integer variable $l \in \mathcal{V}$ by the Rattle integrator [3]:

$$0 = q_k - q_{k+1} + \frac{w_k h_k}{2} \left(\frac{\partial H}{\partial p}(p_{k+1/2}, q_k) + \frac{\partial H}{\partial p}(p_{k+1/2}, q_{k+1}) \right) \quad (11)$$

$$0 = p_k - p_{k+1/2} - \frac{w_k h_k}{2} \left(\frac{\partial H}{\partial q}(p_{k+1/2}, q_k) + \frac{\partial (g_l^h)^T}{\partial q}(q_k) \lambda_k - f(q_k, p_k, u_k) \right) \quad (12)$$

$$0 = w_k g_l^h(q_{k+1}) \quad (13)$$

$$0 = p_{k+1/2} - p_{k+1} - \frac{w_k h_k}{2} \left(\frac{\partial H}{\partial q}(p_{k+1/2}, q_{k+1}) + \frac{\partial (g_l^h)^T}{\partial q}(q_{k+1}) \mu_k - f(q_k, p_k, u_k) \right) \quad (14)$$

$$0 = w_k \frac{\partial (g_l^h)^T}{\partial q}(q_{k+1}) \frac{\partial H}{\partial p}(p_{k+1}, q_{k+1}) \quad (15)$$

Here, the equations (14) represent a projection step with $\mu_k \in \mathbb{R}^{n_{g^h}}$ and the equations (15) represent the holonomic constraints on velocity level.

The first example of an impactive hybrid system that is considered is a double pendulum, where only the first angle is actuated and the second angle is lockable, see Figure 1 (left). In the case that the system with the integer variable $l = 1$ is active, the pendulum is unlocked and g_l^h and $\frac{\partial g_l^h}{\partial q}$ are replaced by zero, such that the equations (13) and (15) vanish. In the case that the system with the integer variable $l = 2$ is active, the pendulum is locked and it holds that $g_l^h(q_{k+1}) = (q_2)_{k+1} - (q_2)_k$, such that the value of the second angle $(q_2)_{k+1}$ does not change if equation (13) is fulfilled. Further integer dependent constraints $g_1(q_k, q_{k+1}) = ((q_1)_k, (q_1)_{k+1}) \leq (\frac{\pi}{2}, \frac{\pi}{2})$ and $g_2(q_k, q_{k+1}) = -((q_1)_k, (q_1)_{k+1}) \leq (\frac{\pi}{2}, \frac{\pi}{2})$ define the domains D_1 and D_2 and assure that the pendulum is locked if the first angle is greater than or equal to $\frac{\pi}{2}$. The boundary constraints (8) and the objective (4) are selected, such that the optimized trajectory describes an upswing maneuver with minimal control effort $\int_I u^2 dt$. Figure 1 (middle and right) represents the results of the optimization using the gradient based IPOPT interior point method [4].

lockable double pendulum

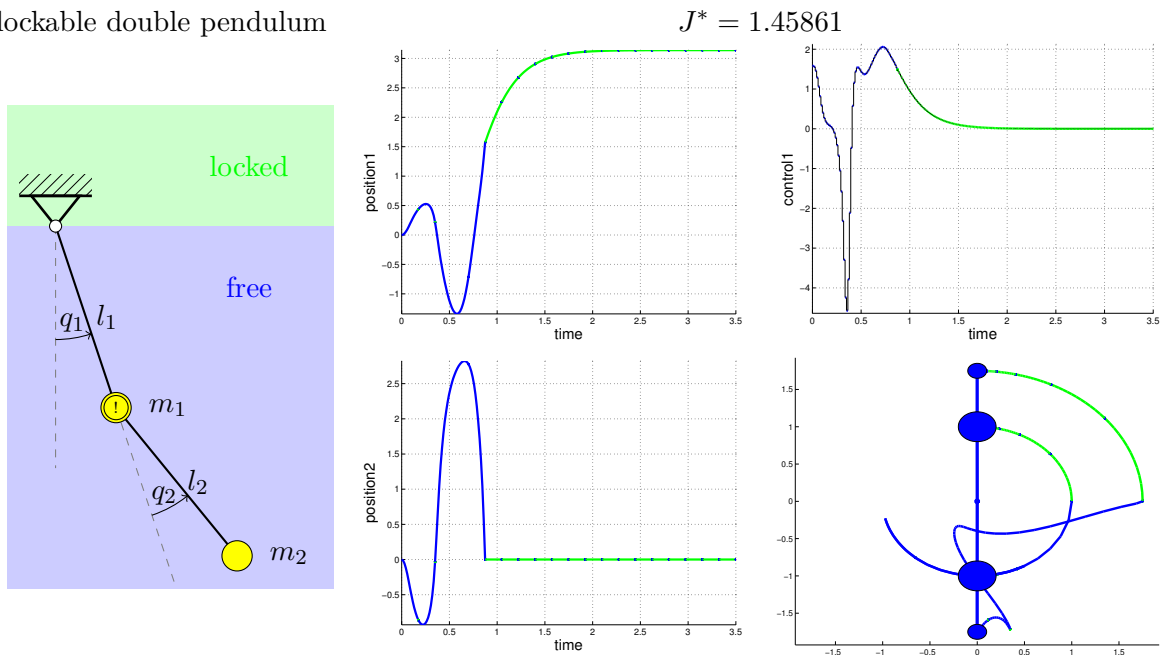


Figure 1: Sketch of the lockable double pendulum (left). Locally optimal discretized state trajectory (middle), control trajectory (top right) and the trajectory of the mass positions (bottom right)

References

- [1] M. Gerdt. *A variable time transformation method for mixed-integer optimal control problems*. Optimal Control Applications and Methods, Vol. 27, No. 3, pp. 169–182, 2006.
- [2] M. Ringkamp, S. Ober-Blöbaum, S. Leyendecker. *On the time transformation of mixed integer optimal control problems using a consistent fixed integer control function*. submitted, 2015
- [3] E. Hairer, C. Lubich, G. Wanner. *Geometric numerical integration: structure-preserving algorithms for ordinary differential equations*. Vol. 31, Springer, 2006
- [4] A. Wächter, L.T. Biegler. *On the implementation of an interior-point filter line-search algorithm for large-scale nonlinear programming*. Mathematical Programming, Vol. 106, No. 1, pp. 25–57, 2006.

Dielectric elastomer actuated multibody systems

Tristan Schlögl, Sigrid Leyendecker

Dielectric elastomer actuators (DEAs), also known as artificial muscles, belong to the group of smart materials. If a voltage is applied to the elastic material, it contracts. The underlying functional principle is based on contractive forces between opposite charges on a plate capacitor, as shown in Figure 1. If the electrodes of the capacitor as well as the insulating material in between are both elastic and not spatially fixed, attractive charges lead to a contraction. Dielectric actuators have a high potential for replacing electrical drives in various systems. They can be used as actuators in

soft robotics, providing safe and robust humanoid systems. A computer model of the time dependent behaviour of this smart material is used to accompany the manufacturing process and provide optimal control for DEA actuated multibody systems.

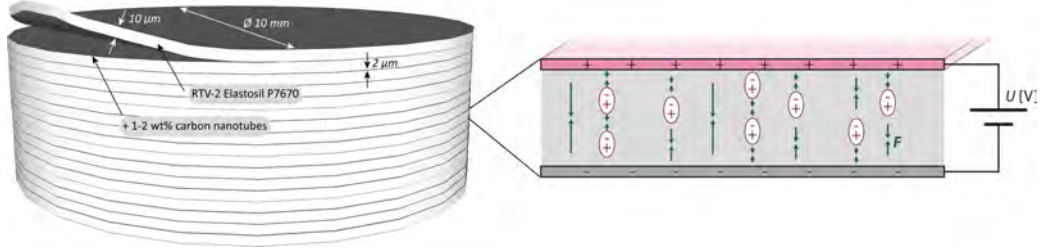


Figure 1: Stacked actuator and the functional principle of a single element

A variational formulation of a three-dimensional, electromechanically fully coupled and time dependent simulation model is presented in [2]. Via finite elements, the model allows to simulate arbitrary geometries of dielectric elastomers including hyperelastic material behaviour and viscoelastic damping. It is based on the Maxwell equations for electrostatics, the mechanical momentum balance and the theory of electromagnetic forces in deformable continua. The actuator model is coupled with a multibody system consisting of rigid bodies and joint connections. This framework allows to simulate multibody systems, e.g. humanoid robots, that are actuated by artificial muscles. The coupling between the finite element model of the muscle and the rigid structure is formulated at position level and enforced by the Lagrange multiplier method, resulting in an index-3 system. A structure preserving integration scheme allows solving the index-3 system directly and with numerical accuracy at position level. Index reduction techniques are not used and there is no erroneous drift in the fulfilment of the constraints. A certain representation of the rigid bodies called director formulation avoids any rotational degrees of freedom and hence numerical instabilities associated with rotations. Additionally, due to the director formulation, all constraints between the finite element model and rigid bodies are linear. Therefore, the whole framework can be formulated in a very modular way.

The discrete Lagrange-d'Alembert principle for constrained systems reads

$$D_1 L_d(\mathbf{q}_n, \mathbf{q}_{n+1}) + D_2 L_d(\mathbf{q}_{n-1}, \mathbf{q}_n) - \mathbf{G}^T(\mathbf{q}_n) \cdot \boldsymbol{\lambda}_n + \mathbf{f}(\mathbf{q}_n, \mathbf{q}_{n+1}) + \mathbf{f}(\mathbf{q}_{n-1}, \mathbf{q}_n) = \mathbf{0} \quad (1a)$$

$$\mathbf{g}(\mathbf{q}_{n+1}) = \mathbf{0} \quad (1b)$$

where L_d is the time discrete Lagrangian, \mathbf{q}_n the discrete configuration at time t_n , \mathbf{G} the Jacobian of the constraints \mathbf{g} and \mathbf{f} the discretised external forces. D_i is the derivative operator with respect to the i -th argument of the succeeding function. The evaluation of (1) yields a non-linear structure preserving time integration scheme [1].

Considering only kinetic and potential energies of the muscle model and introducing the configuration \mathbf{r}_n containing all degrees of freedom of the muscle model at time t_n , namely translations and electric potentials associated with finite element cells, (1a) yields the integration scheme

$$\mathbf{F}_r(\mathbf{r}_{n-1}, \mathbf{r}_n, \mathbf{r}_{n+1}) = \mathbf{0} \quad (2)$$

with the linearised form

$$\mathbf{F}_r + \mathbf{K}_r \cdot \Delta \mathbf{r}_{n+1} = \mathbf{0} \quad (3)$$

where $\mathbf{K}_r = D_3 \mathbf{F}_r$. In contrast to the finite element configuration \mathbf{r} , the configuration \mathbf{s} contains all degrees of freedom of the multibody system. Considering only energies of the multibody system, (1)

yield the integration scheme

$$\mathbf{T}^T(\mathbf{s}_n) \cdot \mathbf{F}_s(\mathbf{s}_{n-1}, \mathbf{s}_n, \mathbf{s}_{n+1}) = \mathbf{0} \quad (4a)$$

$$\mathbf{h}(\mathbf{s}_{n+1}) = \mathbf{0} \quad (4b)$$

where \mathbf{h} are the discrete multibody constraints accounting for joints as well as orthonormality of the directors and \mathbf{T} is the null space matrix eliminating Lagrange multipliers that result from multibody constraints [1]. The corresponding linearised version is given as

$$\begin{pmatrix} \mathbf{T}^T \cdot \mathbf{F}_s \\ \mathbf{h} \end{pmatrix} + \begin{pmatrix} \mathbf{T}^T \cdot \mathbf{K}_s \\ \mathbf{H} \end{pmatrix} \cdot \Delta \mathbf{s}_{n+1} = \mathbf{0} \quad (5)$$

with $\mathbf{K}_s = D_3 \mathbf{F}_s$ and the discrete multibody constraint jacobian $\mathbf{H} = D\mathbf{h}$.

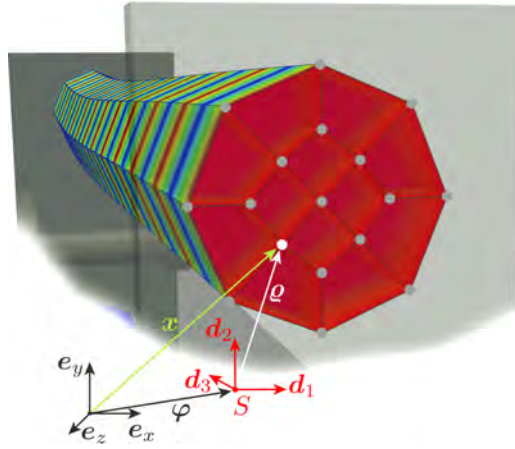


Figure 2: Linear coupling constraints between the finite element muscle model and the multibody system with directors \mathbf{d}_I , $I = 1, 2, 3$, rigid body centre of mass $\boldsymbol{\varphi}$, finite element node position \boldsymbol{x} and coupling location \boldsymbol{q}

The configuration \mathbf{q} of the coupled system is given as

$$\mathbf{q}_n = \begin{pmatrix} \mathbf{r}_n \\ \mathbf{s}_n \end{pmatrix} \quad (6)$$

Because a director formulation is used for the multibody system that avoids the occurrence of rotational degrees of freedom, discrete coupling constraints $\mathbf{g}(\mathbf{r}, \mathbf{s})$ between the muscle model and a rigid body are linear functions of the total configuration \mathbf{q} (see Figure 2) and the associated discrete constraint Jacobian

$$\mathbf{G} = (\mathbf{G}_r \quad \mathbf{G}_s) \quad \text{with} \quad \mathbf{G}_r = D_1 \mathbf{g}(\mathbf{r}, \mathbf{s}) \quad (7) \\ \text{and} \quad \mathbf{G}_s = D_2 \mathbf{g}(\mathbf{r}, \mathbf{s})$$

is constant in time. Evaluating (1) for the coupled system leads to the integration scheme

$$\begin{pmatrix} \mathbf{F}_r - \mathbf{G}_r^T \cdot \boldsymbol{\lambda}_n \\ \mathbf{T}^T \cdot (\mathbf{F}_s - \mathbf{G}_s^T \cdot \boldsymbol{\lambda}_n) \\ \mathbf{h} \\ \mathbf{g} \end{pmatrix} = \mathbf{0} \quad (8)$$

with the linearised form

$$\begin{pmatrix} \mathbf{F}_r - \mathbf{G}_r^T \cdot \boldsymbol{\lambda}_n \\ \mathbf{T}^T \cdot (\mathbf{F}_s - \mathbf{G}_s^T \cdot \boldsymbol{\lambda}_n) \\ \mathbf{h} \\ \mathbf{g} \end{pmatrix} + \begin{pmatrix} \mathbf{K}_r & \mathbf{0} & -\mathbf{G}_r^T \\ \mathbf{0} & \mathbf{T}^T \cdot \mathbf{K}_s & -\mathbf{T}^T \cdot \mathbf{G}_s^T \\ \mathbf{0} & \mathbf{H} & \mathbf{0} \\ \mathbf{G}_r & \mathbf{G}_s & \mathbf{0} \end{pmatrix} \cdot \begin{pmatrix} \Delta \mathbf{r}_{n+1} \\ \Delta \mathbf{s}_{n+1} \\ \Delta \boldsymbol{\lambda}_n \end{pmatrix} = \mathbf{0} \quad (9)$$

with $\boldsymbol{\lambda}_n$ being the Lagrange multipliers of the coupling constraints. Due to the director formulation, the linearised system's matrix is independent of the Lagrange multipliers $\boldsymbol{\lambda}$. The integration scheme presented in (9) is implemented as C++ code using the library deal.II. Figure 3 shows possible motions of different examples.



Figure 3: Numerical examples of a revolute joint (left), a cardan joint (mid) and two serial revolute joints (right)

References

- [1] S. Leyendecker, J.E. Marsden, and M. Ortiz. *Variational integrators for constrained dynamical systems*. Z. Angew. Math. Mech., Vol. 88, pp. 677-708, 2008.
- [2] T. Schlögl, and S. Leyendecker. *Electrostatic-viscoelastic finite element model of dielectric actuators*. Comput. Methods Appl. Mech. Engrg., Vol. 299, pp. 421-439, 2016.

Construction and analysis of higher order variational integrators for dynamical systems with holonomic constraints

Theresa Wenger, Sina Ober-Blöbaum, Sigrid Leyendecker

Variational integrators of higher order for systems with holonomic constraints are constructed and analyzed. The idea builds up on the variational integrators of higher order for unconstrained systems in [3] and on the constrained Galerkin methods, that are presented in [2]. The integrators base on a discrete version of the variational principle of Lagrangian mechanics. Consider an n -dimensional mechanical system defined on the configuration manifold $Q \subseteq \mathbb{R}^n$ with configuration vector $q \in Q$ and velocity vector $\dot{q}(t) \in T_{q(t)}Q$. The variable t denotes the time in the interval $t = [t_0, t_N]$. The Lagrangian L of a mechanical system is the difference of the kinetic energy T and the potential V . In presence of holonomic constraints $g(q) \in \mathbb{R}^m$, the scalar product $-g(q) \cdot \lambda$ augments the Lagrangian, whereby $\lambda \in \mathbb{R}^m$ is the Lagrange multiplier. The so called augmented Lagrangian $\bar{L} : TQ \times \mathbb{R}^m \rightarrow \mathbb{R}$ is defined by

$$\bar{L}(q, \dot{q}, \lambda) = L(q, \dot{q}) - g(q) \cdot \lambda$$

The approach is, to approximate the continuous curves of the configuration q , the velocity \dot{q} and the Lagrange multiplier λ on the time interval $[0, h]$ via the polynomials q_d , \dot{q}_d and λ_d . The polynomial $q_d(t; q_k, h)$, $t \in [0, h]$, is uniquely defined by $s + 1$ configurations $q_k = (q_k^0, \dots, q_k^s) \in Q^{s+1}$ at $s + 1$ control points $0 = d_0 < d_1 < \dots < d_{s-1} < d_s = 1$, such that the polynomial passes through each q_k^ν at the time $d_\nu h$, $\nu = 0, \dots, s$. Analogously, $w + 1$ Lagrange-multipliers $\lambda_k = (\lambda_k^0, \dots, \lambda_k^w) \in (\mathbb{R}^m)^{w+1}$ at $w + 1$ control points $\tilde{d}_0 = 0 < \tilde{d}_1 < \dots < \tilde{d}_{w-1} < \tilde{d}_w = 1$ uniquely define the polynomial $\lambda_d(t; \lambda_k, h)$, $t \in [0, h]$. To get continuous approximations of q and λ on $[t_0, t_N]$, with $[t_0, t_N] = \bigcup_{k=0}^{N-1} [kh, (k+1)h]$, the conditions $q_k^s = q_{k+1}^0$, $k = 0, \dots, N - 2$ and $\lambda_k^w = \lambda_{k+1}^0$, $k = 0, \dots, N - 2$ must be fulfilled. Note, that the control points d_j , $j = 0, \dots, s$ of q_d do not have to match the control points \tilde{d}_j , $j = 0, \dots, w$ of λ_d , neither has the degree w of the polynomial λ_d to equal the degree s of q_d . The splitting of the augmented Lagrangian in the two parts Lagrangian and scalar product $g(q) \cdot \lambda$ enables the use of different quadrature formulas for each part. The discrete Lagrangian L_d approximates the integral in $[0, h]$ of the Lagrangian via the quadrature formula $(c_i, b_i)_{i=1}^r$ of order $ordL$. g_d is the approximation of the integral in $[0, h]$ of $g(q) \cdot \lambda$ via the quadrature formula $(e_i, f_i)_{i=1}^z$ of order $ordZ$. The quadrature formulas are w.r.t. the time $[0, 1]$ with quadrature nodes c_i respectively f_i and the associated weights b_i respectively e_i , in particular the Gauss and Lobatto quadrature are used here. \bar{S}_d is the approximation of the augmented action integral \bar{S} , i.e. the integral in $[t_0, t_N]$ of the augmented Lagrangian. Requiring stationarity of \bar{S}_d yields the discrete Euler-Lagrange equations. Assume the Lagrangian L is regular and the order $ordL$ is high enough, such that the discrete Lagrangian flow is well defined. Further assumptions such that g_d is approximated via the Lobatto quadrature and the $w + 1$ control points of λ_d match the quadrature nodes f_i , $i = 1, \dots, z$, with $z = w + 1$, and $s \geq w$, ensure that the number of unknowns equals the number of linear independent equations in the discrete Euler-Lagrange equations and yield stiffly accurate integrators. Under these assumptions, the discrete augmented Lagrangian reads

$$\bar{L}_d(q_k, \lambda_k) = L_d(q_k) - g_d(q_k, \lambda_k) \quad k = 0, \dots, N - 1 \quad (1)$$

with

$$L_d(q_k) = h \sum_{i=1}^r b_i L(q_d(c_i h; q_k), \dot{q}_d(c_i h; q_k)) \quad (2)$$

$$g_d(q_k, \lambda_k) = h \sum_{i=0}^w e_{i+1} \left[g(q_d(\tilde{d}_i h; q_k)) \cdot \lambda_k^i \right] \quad (3)$$

The corresponding discrete Euler-Lagrange equations are constrained variational integrators. The preservation properties of these variational integrators are analysed and verified by numerical examples. They are symplectic and therefore have a excellent energy long-time behaviour. Furthermore, they preserve momentum maps proofed via the discrete Noether-theorem for constrained systems extended to constrained variational integrators of higher order. It is shown, that the constructed variational integrators are symmetric on configuration level, but not necessarily on momentum level, as the hidden constraints $\frac{\partial g}{\partial q}(q) \dot{q} = 0$ typically fail to be satisfied. The convergence orders of the variational integrators are investigated numerically. The following remarks are valid only, when $s = w$ or $s = w + 1$ and $ordL \geq 2s$. The results for the convergence order of the configuration q , briefly named $ord(q)$, can be summarized as follows. It must be distinguished between calculating L_d (2) via the Lobatto or via the Gauss quadrature. Thus, the orders $ordL$ and $ordZ$ of the quadrature formulas determine

$$\begin{aligned} L_d \text{ via Gauss quadrature} & \quad ord(q) = \min(ordL, ordZ) = \min(2s, 2r, 2w) \\ L_d \text{ via Lobatto quadrature} & \quad ord(q) = \min(ordL, ordZ) = \min(2s, 2r - 2, 2w) \end{aligned}$$

as the resulting order of the variational integrator in q . Furthermore, the configuration q is super convergent of order $2s$, when $r \geq s$ (approximating L_d (2) via the Gauss quadrature) respectively

$r \geq s + 1$ (approximating L_d (2) via the Lobatto quadrature). The order of the Lagrange multiplier λ , $\text{ord}(\lambda)$, is reduced compared to the order of the configuration q . The convergence order of the momentum p , $\text{ord}(p)$, is also mostly smaller than that of the configuration q . Note, that the momentum p is calculated in a post-processing step via the discrete Legendre transform. There is a relation between the degree w of the polynomial λ_d and the convergence orders of the Lagrange multiplier λ and the momentum p recognizable.

$$\begin{aligned} w \text{ even:} & \quad \text{ord}(p) = w + 2 \quad \text{ord}(\lambda) = w \\ w \text{ uneven:} & \quad \text{ord}(p) = w + 1 \quad \text{ord}(\lambda) = w + 1 \end{aligned}$$

Moreover it is significant, that all orders are even. The constructed variational integrators are shown to be symmetric in q , but not in p and in λ . However, the numerical examination reveals even orders for q , p and λ . Furthermore, when s is greater than $w + 1$, order reduction in q , p and λ occurs. The limitation of the order $\text{ord}Z$ to $2w$ might be a reason.

The discrete augmented Lagrangian (1) can serve as a generating function for the SPARK integrators of [1]. However, in [1] the SPARK integrator is applied to a system of index 2 ODAEs. Furthermore, in contrast to [2] and [1], the restriction $r = s$ for the quadrature nodes for approximating the integral of the Lagrangian is dropped here as it is in [3] for the unconstrained systems.

References

- [1] L.O. Jay. *Specialized partitioned additive Runge-Kutta methods for systems of overdetermined daes with holonomic constraints*. SIAM Journal on Numerical Analysis, Vol. 45(5), pp. 1814-1842, 2007.
- [2] J.E. Marsden, and M. West. *Discrete mechanics and variational integrators*. Acta Numerica 2001, Vol. 10, pp. 357-514, 2001.
- [3] S. Ober-Blöbaum, and N. Saake. *Construction and analysis of higher order Galerkin variational integrators*. Advances in Computational Mathematics, Vol. 41, pp. 955-986, 2014.

4 Activities

4.1 Teaching

Wintersemester 2015/2016

Biomechanik der Bewegung (MT) Vorlesung + Übung		H. Lang
Dynamik starrer Körper (MB, ME, WING, IP, BPT, CE) Vorlesung Übung + Tutorium		H. Lang D. Budday, D. Glaas T. Leitz, M. Ringkamp T. Schlögl, T. Wenger
Mehrkörperdynamik (MB, ME, WING, TM, BPT) Vorlesung Übung		H. Lang T. Wenger
Dynamisches Praktikum – Modellierung, Simulation und Experiment (MB, ME, WING, IP, BPT)		D. Budday, D. Glaas T. Leitz, M. Ringkamp T. Schlögl, T. Wenger

Sommersemester 2015

Biomechanik (MT, MA, GPP) Vorlesung + Übung geprüft	61 + 21 (WS 2014/2015)	H. Lang
Dynamik nichtlinearer Balken (MB, M, Ph, CE, ME, WING) Vorlesung + Übung geprüft	14	H. Lang, M. Ringkamp
Geometrische numerische Integration (MB, ME, WING, BPT) Vorlesung Übung geprüft	6 + 1 (WS 2014/2015)	S. Leyendecker T. Wenger
Statik und Festigkeitslehre (CBI, CE, ET, LSE, ME, MWT, IP, MT, CEN, BPT) Vorlesung Übung + Tutorium geprüft	497	S. Leyendecker T. Gail, T. Wenger D. Budday, T. Schlögl T. Leitz, M. Ringkamp

Theoretische Dynamik II
(M, TM, MB, ME, CE, BPT, WING, Ph)
Vorlesung + Übung
geprüft 12 + 2 (WS 2014/2015) H. Lang

Rechnerunterstützte Produktentwicklung (RPE)
Versuch 6: Mehrkörpersimulation in Simulink
(MB, ME, WING) Praktikum
Teilnehmer 64
T. Gail, T. Wenger
T. Leitz, M. Ringkamp
T. Schlögl

Wintersemester 2014/2015

Biomechanik der Bewegung (MT)
Vorlesung + Übung
geprüft 35 + 14 (SS 2015) H. Lang

Dynamik starrer Körper (MB, ME, WING, IP, BPT, CE)
Vorlesung
Übung + Tutorium
geprüft 493 + 154 (SS 2015)
S. Leyendecker
D. Budday, O.T. Kosmas
T. Leitz, M. Ringkamp
N. Bach, T. Gail, T. Schlögl

Mehrkörperdynamik (MB, ME, WING, TM, BPT, CE)
Vorlesung
Übung
geprüft 39 + 6 (SS 2015)
S. Leyendecker
O.T. Kosmas

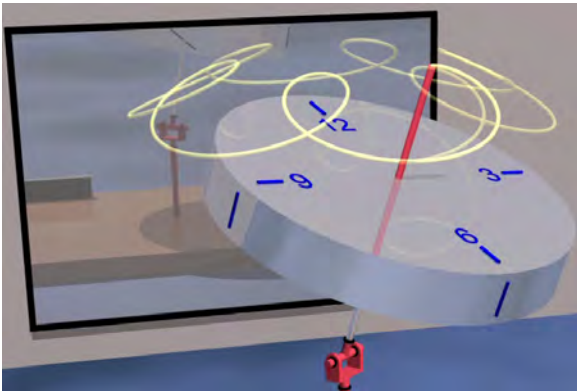
Numerische Methoden in der Mechanik
(MB, ME, WING, TM, CE, BPT)
Vorlesung + Übung
geprüft 40 + 15 (SS 2015) H. Lang

Theoretische Dynamik I (MB, ME, WING, TM, BPT)
Vorlesung + Übung
geprüft 22 + 14 (SS 2015) H. Lang, D. Budday

4.2 Dynamical laboratory – modeling, simulation and experiment

The dynamical laboratory – modeling, simulation and experiment addresses all students of the Technical Faculty of the FAU Erlangen-Nuremberg. The aim of the practical course is to develop mathematical models of fundamental dynamical systems to simulate them numerically and the results are compared to measurements from the real mechanical system. Here, the students learn both the enormous possibilities of computer based modeling and its limitations. The course contains one central programming experiment and six experiments at the real existing objects, including the corresponding numerical simulation.

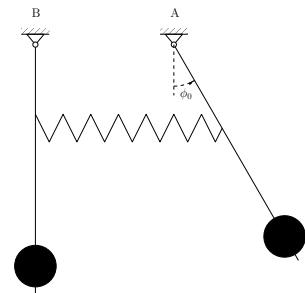
Programming training



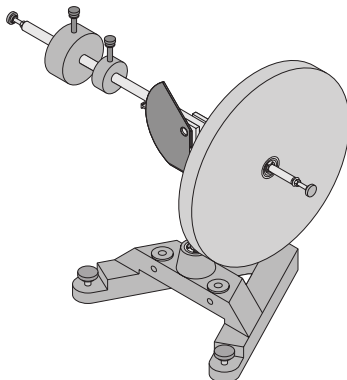
During the central programming training, the students learn to deal with MATLAB and Simulink. Here, prototypically, two examples are considered, the classical Lagrange top in MATLAB and a distance controller in Simulink. The Lagrange top exhibits non trivial nutation while performing precession around the vertical direction of gravitational acceleration. The trajectory of the symmetry axis might even build loops or cusps.

Beating pendulums

The experiment beating pendulums is about two heavy pendulums that are connected with a soft spring. The theory allows a complete analytical solution of the linearised equations of motion. As an alternative, the solution trajectories might be gained by numerical time integration. The results belonging to three typical initial conditions are monitored at two coupled pendulums in the laboratory. Especially, the dynamic beat phenomenon is inspected.



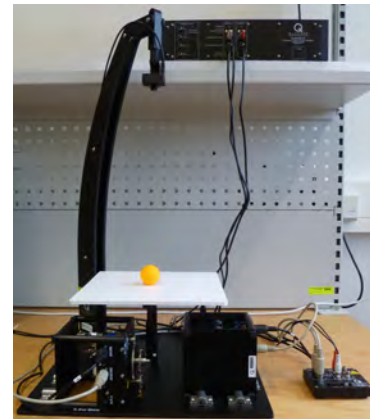
Gyroscope



In the experiment gyroscope, the force-free and heavy top are investigated. The experimental setup constitutes a multibody system that is modeled by Lagrangian mechanics and simulated in MATLAB. In the laboratory, the motion of the gyroscope is captured via angle sensors. The measured trajectories are compared to the simulation, which validates the model.

Ball balancer

The system ball balancer basically consists of a plate on which a ball is free to roll. Two servomotors may incline the plate. A camera situated above the plate detects the position of the ball. The goal is to implement a regulator that controls the motion of the ball. Preliminarily, the system is modeled. To that end, the equations of motion of the ball and the differential equations of the motors are derived. The fundamentals of control theory are inspected, and a PD-controller is created. During the experiment, the controller is tested and improved. Possible reasons for discrepancies between theory and practice are discussed.



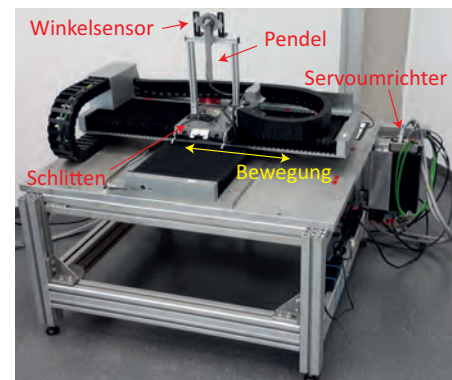
Robot arm



The experiment robot arm serves as an introduction into multibody dynamics. Here, the frequently used Denavit-Hartenberg conventions are introduced, which are suitable to derive the kinematic equations systematically. The transformation matrices are used in order to compute the position and orientation of the robot arm for arbitrary joint angles in space. Experiments with a virtual model in MATLAB and a real robot arm illustrate the practical use of the methods described.

Inverse pendulum

The experiment inverse pendulum concerns a swing-up maneuver of a pendulum on a slinging carriage from the lower (stable) into the upper (unstable) static equilibrium position. Especially, the built-in incremental path sensors are considered, which are explored by an oscilloscope. With the aid of MATLAB, a dynamic model of the machine is solved structure-preservingly and compared to measurements in order to identify an appropriate friction model. A carriage motion that drives the pendulum into the upper position is obtained by optimal control algorithms. Finally, that motion is tested on the real system.



Balancing robot



The experiment illustrates modeling, numerical computation and reality at the example of a Lego robot that is self-balancing on two wheels. Preparatively, the students are concerned with modeling the robot as a multi-body system, the derivation of the equations of motion and the basic knowledge in control theory. Then, they perform simulations and compare the results to measurements. Thereby, several aspects as the dynamic behaviour, stability, robustness, controlling accuracy and possible sources of error are to be discussed.

4.3 Theses

PhD theses

- Michael Koch
Structure preserving simulation of non-smooth dynamics and optimal control

Master theses

- Katrin Ederer
Dynamische Simulation der Bewegungen eines biomechanischen Armmodells mit Prothese
- Daniel Glaas
Optimal feedback control for constrained mechanical systems
- Hannah Laube
Numerische Aufwandsbestimmung verschiedener Formulierungen der Bewegungsgleichung am Beispiel des ebenen Kirchhoff-Balkens
- Uday Phutane
On the comparison of different muscle model dynamics using variational integrators
- Jochen Uhlig
Polyzentrische Knieprothesen – Kinematische Analyse und Modellierung als Mehrkörpersystem mit Zwangsbedingungen
- Theresa Wenger
Variationelle Integratoren gemischter Ordnungen für dynamische Systeme mit gesplitteten Potentialen

Project theses

- Markus Eisentraut
Kreiseldynamik: Theorie, Simulation, Experiment
- Johann Penner
Charakterisierung von Reibmodellen zur Simulation eines inversen Pendels
- Dominik Reichl
Zur inversen Dynamik eines Roboterarms unter Einwirkung von Reibung

- Johannes Rudolph
Passive shape undulations in underwater locomotion

Bachelor theses

- Theresa Ach
Simulation of a servo constrained rotary crane using variational integrators
- Jonas Fertsch
Experimentelle Analyse des NXTway-GS-Roboter
- Björn Hübner
Vergleich verschiedener Muskelmodelle
- Michael Jäger
Modellierung eines keltischen Wackelsteins unter Verwendung verschiedener Parametrisierungen der Rotationsfreiheitsgrade
- Judith Probst
Modellierung und Optimierung der Abrollbewegung eines Mehrkörpersystems
- Miriam Scharnagel
Modellbildung und inverse Dynamik eines Roboterarms
- Cosima Schellenberger
Viskoelastische Cosserat-Balken aus Kelvin-Voigt-Material zur numerischen Simulation von Sehnen - Vergleich mit dem 3D-Kontinuum
- Anja Thielecke
Numerische Simulation der Dynamik eines Windspiels

4.4 Seminar for mechanics

together with the Chair of Applied Mechanics LTM

- 02.02.2015 Jaroslav Vondřejc
Faculty of Applied Sciences, University of West Bohemia, Plzen, Czech Republic
FFT-based Galerkin method for a reliable determination of homogenized material properties
- 19.02.2015 Lukas Allabar
Bachelor thesis, Chair of Applied Dynamics, University of Erlangen-Nuremberg
Structure preserving simulation of a planar slider crank with translational joint clearance
- 19.02.2015 Daniel Glaas
Master thesis, Chair of Applied Dynamics, University of Erlangen-Nuremberg
Optimal feedback control for constrained mechanical systems
- 19.02.2015 Björn Hübner
Bachelor thesis, Chair of Applied Dynamics, University of Erlangen-Nuremberg
Vergleich verschiedener Muskelmodelle

- 19.02.2015 Hannah Laube
Project- und Master thesis, Chair of Applied Dynamics, University of Erlangen-Nuremberg
Numerische Aufwandsbestimmung verschiedener Formulierungen der Bewegungsgleichung am Beispiel des ebenen Kirchhoff-Balkens
- 19.02.2015 Judith Probst
Bachelor thesis, Chair of Applied Dynamics, University of Erlangen-Nuremberg
Modellierung und Optimierung der Abrollbewegung eines Mehrkrpersystems
- 16.03.2015 Stephan Rudykh
Department of Aerospace Engineering, Technion – Institute of Technology, Israel
Micromechanics of soft dielectric elastomers and magnetorheological elastomers
- 16.04.2015 Miriam Scharnagel
Bachelor thesis, Chair of Applied Dynamics, University of Erlangen-Nuremberg
Modellbildung und inverse Dynamik eines Roboterarms
- 16.04.2015 Jochen Uhlig
Master thesis, Chair of Applied Dynamics, University of Erlangen-Nuremberg
Polyzentrische Knieprothesen – Kinematische Analyse und Modellierung als Mehrkrpersystem mit Zwangsbedingungen
- 27.04.2015 Kateryna Plaksiy
Department of Applied Mathematics, NTI, Kharkiv Polytechnic Institute, Ukraine
Dynamics of nonlinear dissipative systems in the vicinity of resonance
- 20.05.2015 Johannes Rudolph
Project thesis, Chair of Applied Dynamics, University of Erlangen-Nuremberg
Passive shape undulations in underwater locomotion
- 15.06.2015 Andrew McBride
Centre for Research in Computational and Applied Mechanics, University of Cape Town, South Africa
Computational and theoretical aspects of a grain-boundary model that accounts for grain misorientation and grain-boundary orientation
- 22.06.2015 Valery Levitas
Departments of Aerospace Engineering, Iowa State University, USA
Interaction between phase transformations and dislocations at the nanoscale: Phase field approach
- 20.07.2015 Anja Thielecke
Bachelor thesis, Chair of Applied Dynamics, University of Erlangen-Nuremberg
Numerische Simulation der Dynamik eines Windspiels
- 27.08.2015 Dominik Reichl
Project thesis, Chair of Applied Dynamics, University of Erlangen-Nuremberg
Zur inversen Dynamik eines Roboterarms unter Einwirkung von Reibung

- 02.09.2015 Theresa Ach
Bachelor thesis, Chair of Applied Dynamics, University of Erlangen-Nuremberg
Simulation of a servo constrained rotary crane using variational integrators
- 24.09.2015 Michael Jäger
Bachelor thesis, Chair of Applied Dynamics, University of Erlangen-Nuremberg
Modellierung eines keltischen Wackelsteins unter Verwendung verschiedener Parametrisierungen der Rotationsfreiheitsgrade
- 29.09.2015 Michael Koch
PhD thesis, Chair of Applied Dynamics, University of Erlangen-Nuremberg
Structure preserving simulation of non-smooth dynamics and optimal control
- 07.10.2015 Johann Penner
Project thesis, Chair of Applied Dynamics, University of Erlangen-Nuremberg
Charakterisierung von Reibmodellen zur Simulation eines inversen Pendels
- 10.11.2015 Katrin Ederer
Master thesis, Chair of Applied Dynamics, University of Erlangen-Nuremberg
Dynamische Simulation der Bewegungen eines biomechanischen Armmodells mit Prothese
- 10.11.2015 Jonas Fertsch
Bachelor thesis, Chair of Applied Dynamics, University of Erlangen-Nuremberg
Experimentelle Analyse des NXTway-GS-Roboter
- 20.11.2015 Uday Phuthane
Master thesis, Chair of Applied Dynamics, University of Erlangen-Nuremberg
On the comparison of different muscle model dynamics using variational integrators
- 30.11.2015 Krishnendu Haldar
Institute of Mechanics, TU Dortmund
Discrete Symmetry and Modeling of Magnetic Shape Memory Alloys
- 03.12.2015 Markus Eisentraudt
Project thesis, Chair of Applied Dynamics, University of Erlangen-Nuremberg
Kreiseldynamik: Theorie, Simulation, Experiment

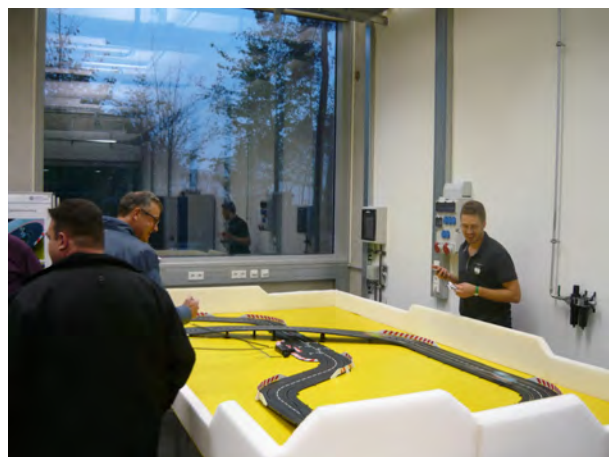
4.5 Editorial activities

Advisory and editorial board memberships Since January 2014, Sigrid Leyendecker is a member of the advisory board of the scientific journal *Multibody System Dynamics*, Springer.

4.6 Long night of science



On October 24, 2015, the ‘Long night of science’ (‘Lange Nacht der Wissenschaften’) took place at many scientific institutions spread around the cities of Nuremberg, Erlangen, and Fuerth for the seventh time since 2003. During the early night between 6 p.m. and 1 a.m., interested people had the opportunity to inform themselves at universities, non-university research institutes, companies and other institutions about actual topics in research and development. The Chair of Applied Dynamics participated and showed interesting experiments in its laboratories, such as the beating phenomenon for pendulums, the conservation of angular momentum, optimal control for an inverted pendulum, a self-balancing robot and a Carrera race course (the exhibited posters are presented on the following pages). People had the chance to execute most of the mechanical experiments on their own, e.g. to feel forces, torques, angular velocity and acceleration experienced on a chair. Some exhibits were well suited for children such as to try to ‘invert’ a pendulum simply by controlling with a joystick without the help of numerical control algorithms. The atmosphere was very nice and the resonance extremely positive, such that the LTD is looking forward to attend the next ‘Long night of science’ in 2017.



Carrera-Bahn ein spielerisches Experiment zur Optimalsteuerung

Herausforderungen

- Start-Ziel-Gerade
- Haarnadel-Kurve
- Überfahrt
- Spurwechsel
- Steilkurve



Spielregeln

Um Ihr Können an der Carrera-Bahn zu testen, gibt es 2 Möglichkeiten.

1. Fahrer gegen Fahrer
Treten Sie im direkten Duell gegeneinander an und finden Sie heraus, wer durch schnelles Fahren und taktisches Können die Nase am Ende vorne hat. Nach dem Startsignal gilt es, 2 Minuten lang so viel Strecke wie möglich zu absolvieren.
2. Kampf gegen die Uhr
Hier gilt es, eine möglichst schnelle Runde zu absolvieren. Sie können die Bahn frei wählen und beliebig die Spur wechseln, am Ende zählt die beste Runde aus 3 Versuchen. Gewertet wird dabei mit einem fliegendem Start.
Zu jeder vollen Stunde gibt es für den Fahrer der Stundenbestzeit einen kleinen Preis.

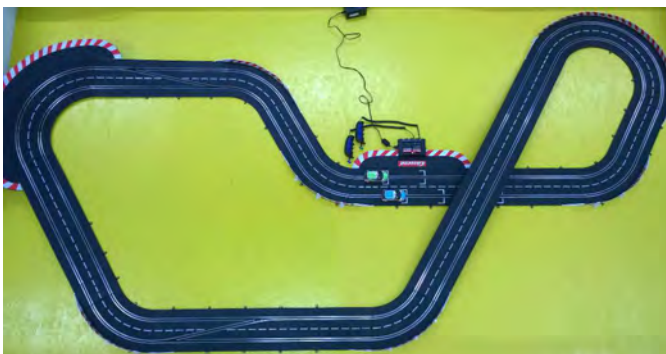


aktuelle Stundenbestzeit

Forschungsaspekte

Mithilfe der Carrera-Bahn wird das Zusammenspiel einiger Forschungsaspekte des Lehrstuhls anhand eines praktischen Beispiels getestet.

- Optimalsteuerung
Ausgehend von einer umfassenden Beschreibung der Fahrdynamik eines Carrera-Autos und des eindimensionalen Steuersignals (Handregler) wird in einer Simulation eine optimale Bewegung und Steuerung berechnet.
Dies entspricht dem Herantasten des Menschen an eine möglichst schnelle Rundenzeit durch mehrmaliges Probieren.
- Positionserkennung
Für die Interaktion in Echtzeit mit dem System ist es vor allem notwendig, eine genau Kenntnis über den aktuellen Ort und die Geschwindigkeit des Wagens zu haben. Dies geschieht mittels einer Kamera, die zentral über der Bahn montiert wird.
- Regelung
Weicht der aktuelle Zustand des Wagens von der optimalen Bewegung ab, so wird der Wagen durch Regelalgorithmen an seine optimale Fahrt angenähert.



Drehimpulserhaltung und Lagrange-Kreisel

Drehimpulserhaltung

Drehimpulserhaltung ist zunächst unintuitiv. Man kann sie in Drehstuhlexperimenten am eigenen Leib erfahren.

1. Man rotiert mit der Winkelgeschwindigkeit ω

auf dem Drehstuhl mit weit ausgebreiteten Armen und schweren Hanteln in den Händen. Die vertikale Komponente des Drehimpulses

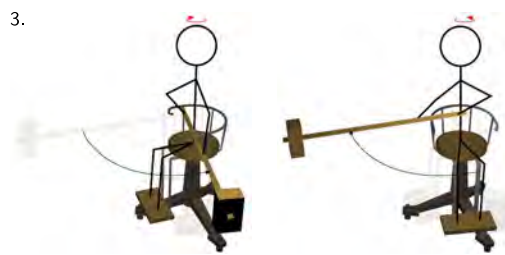
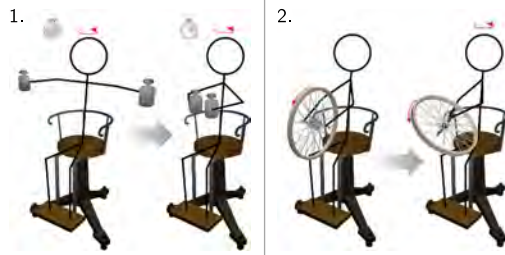
$$L_z = \text{konstant}$$

bleibt erhalten, wenn man die Arme zu sich heranzieht. Damit wird das Trägheitsmoment Θ_z um die vertikale Drehachse kleiner. Folglich muss wegen

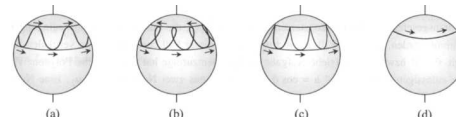
$$L_z = \Theta_z \omega = \text{konstant}$$

die Rotationsgeschwindigkeit ω zunehmen.

2. Hält man das rotierende Rad vertikal, so ist die vertikale Komponente des Gesamtdrehimpulses exakt Null. Dies muss auch so bleiben, wenn man das Rad in die horizontale Position bewegt. Da nun das Rad mit seiner positiven Vertikalkomponente zum Gesamtdrehimpuls beiträgt, muss sich der Drehstuhl in entgegengesetzter Richtung drehen, damit die Vertikalkomponente des Gesamtdrehimpulses weiterhin Null ist.
3. In der ruhenden Position ist der gesamte Drehimpuls L gleich Null. Bewegt man den schweren Hammer nach rechts bzw. nach links, so muss der Drehstuhl sich nach links bzw. nach rechts drehen, damit weiterhin in Summe $L = 0$ gilt.



Trajektorie der Figurenachse



Quelle: 'Mehrkörpersysteme: Eine Einführung in die Kinematik und Dynamik von Systemen starrer Körper' – Christof Wessels

Lagrange-Kreisel

Nutation und Präzession

Der Massenmittelpunkt der Scheibe beschreibt, je nach Anfangsbedingungen, die in (a), (b), (c) und (d) dargestellten Figurenachsen. Die Bewegung um die vertikale Achse wird Präzession (Fortschreiten) und die Auf- und Abbewegung wird Nutation (Nicken) genannt.

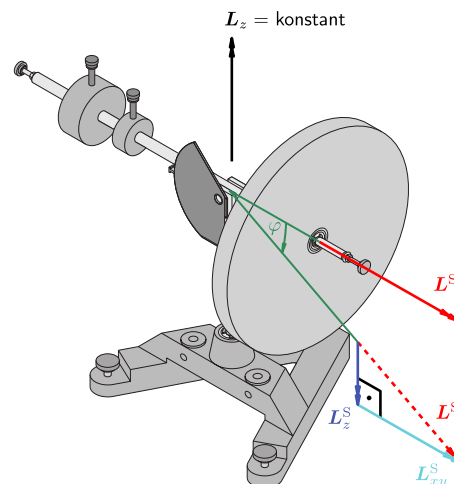
Drehimpulserhaltung

Die oben beschriebene Drehimpulserhaltung ist der Grund dafür, dass der Lagrange-Kreisel das bekannte Bewegungsmuster aus Nutation und Präzession aufweist.

Die vertikale Komponente des Gesamtdrehimpulses ist erhalten

$$L_z = \text{konstant}$$

Bewegt sich die Kreiselscheibe nun aufgrund der Gewichtskraft um den Winkel φ nach unten, so ändert sich die Drehung des Gesamtsystems, um den nun vorhandenen vertikalen Anteil des Drehimpulses der Kreiselscheibe L_z^S auszugleichen.



Schwebung

Beispiel zweier schwebender Pendel

Schwebung

Die Schwebung tritt bei Überlagerung von zwei Schwingungen mit nahe beieinander liegenden Kreisfrequenzen auf. Sie führt zu periodischen Auslöschungen und Verstärkungen der Schwingungsamplitude.

physikalisches Pendel

- ein Freiheitsgrad
- Bewegungsdifferentialgleichung
 $\ddot{\varphi} + \omega_0^2 \varphi = 0$
- Schwingung mit Kreisfrequenz ω_0

durch Feder gekoppelte Pendel

- zwei Freiheitsgrade
- Bewegungsdifferentialgleichungen
 $(\ddot{\phi} + \ddot{\psi}) + \omega_0^2(\phi + \psi) = 0$
 $(\ddot{\phi} - \ddot{\psi}) + \omega_1^2(\phi - \psi) = 0$
- Schwingung mit Kreisfrequenzen ω_0 und ω_1
- $\omega_1 = \sqrt{\omega_0^2 + D_{Feder}}$

Gleichtakt

- Anfangslage – beide Pendel um den gleichen Winkel ausgelenkt
- keine Kraft in Koppelfeder
- Schwingung beider Pendel mit Kreisfrequenz ω_0

Gegentakt

- Anfangslage – beide Pendel entgegengesetzt um den gleichen Winkel ausgelenkt
- maximale Kraft in Koppelfeder
- Schwingung beider Pendel mit Kreisfrequenz ω_1

Schwebung

- Anfangslage – nur ein Pendel ausgelenkt
- Kraft in Koppelfeder
- Überlagerung der beiden Schwingungen mit Kreisfrequenzen ω_0 und ω_1
- jedes Pendel kommt immer wieder kurz zum Stillstand



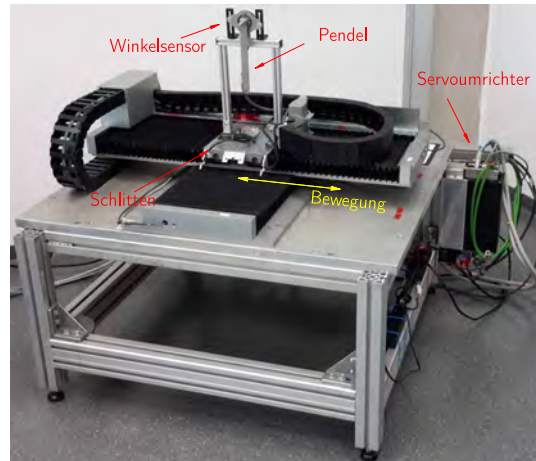
Inverses Pendel – Mensch gegen Maschine

Schwingen Sie das Pendel mit dem Joystick auf!

Das Pendel hat (theoretisch) zwei Ruhelagen. Während es aufgrund der Schwerkraft von alleine nach unten hängt, ist die obere Gleichgewichtslage instabil. Ohne weiteren Eingriff führen kleinste Störungen dazu, dass es wieder nach unten fällt. Wie kann man das Pendel oben halten? Und wie bekommt man es überhaupt nach oben? Von Hand ist das sehr schwierig.

unteraktuierte Systeme

Warum ist es so schwer, das Pendel von Hand aufzuschwingen? Die relevante Bewegung, also die Drehung des Pendels, lässt sich nicht direkt beeinflussen. Das Pendel wird indirekt, durch die Bewegung des Schlittens, in Schwingung versetzt. Man spricht von einem unteraktuierten System.



Computermodell zur Beschreibung der schnellen Pendeldynamik

Um mit dem Computer zu berechnen, wie sich der Schlitten bewegen muss, damit das Pendel aufschwingt, braucht man ein möglichst genaues mathematisches Modell der Anlage. Eine Herausforderung liegt darin, die komplexen Reibphänomene zu beschreiben, welche bei der Bewegung des Pendels auftreten. Methoden der Optimalsteuerung liefern dann die benötigte Schlittenbewegung, um das Pendel in die obere, instabile Ruhelage zu führen – so die Theorie.

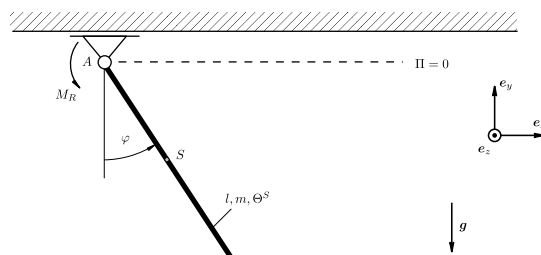
in der Theorie ist die Praxis ideal

Modelle sind immer Idealisierungen komplexer Vorgänge in der Wirklichkeit. Kein mathematisches Modell wird die Anlage perfekt beschreiben. Lagerungen verschleifen, Eigenschaften von Schmiermitteln sind temperaturabhängig, Fertigungstoleranzen sind unvermeidbar. Dazu kommen unvorhergesehene Störungen, wie Erschütterungen des Bodens oder ein Windstoß. Ob das noch was wird mit dem Aufschwingen?

Kaskadenregelung

Für den Versuch wurde eine Kaskadenregelung verwendet. Dabei handelt es sich um eine Verschachtelung mehrerer Regelkreise. Ein innerer Regelkreis reagiert sehr schnell und hält das Pendel in der oberen Ruhelage, ohne dabei die aktuelle Schlittenposition zu berücksichtigen. Ein etwas langsamerer äußerer Regelkreis führt den Schlitten wieder zur Mitte zurück. So kann das System auf neue Störungen reagieren, ohne dass der Schlitten seinem Endanschlag zu nahe kommt.

Modell des Pendels auf dem Schlitten



Steuerung und Regelung

Während die reine Steuerung des Systems unbeeindruckt äußerer Einflüsse ihren Dienst verrichtet, reagiert die Regelung auf externe Störungen. Treten bei der Steuerung Abweichungen zwischen Ist- und Soll-Zustand auf, greift die Regelung ein und stabilisiert die Lage. In diesem Fall hält die Regelung das Pendel in der oberen Ruhelage, nachdem es die Optimalsteuerung in deren Nähe gebracht hat. Ob das jemand mit dem Joystick geschafft hätte?

5 Publications

5.1 Reviewed journal publications

1. D. Budday, S. Leyendecker, and H. van den Bedem. *Geometric analysis characterizes molecular rigidity in generic and non-generic protein configurations*. Journal of the Mechanics and Physics of Solids, Vol. 83, pp. 736-47, 2015.
2. F. Demoures, F. Gay-Balmaz, S. Leyendecker, S. Ober-Blöbaum, T.S. Ratiu, and Y. Weinand. *Discrete variational Lie group formulation of geometrically exact beam dynamics*. Numerische Mathematik, Vol. 130, pp. 73-123, 2015.
3. T. Schlögl, and S. Leyendecker. *Electrostatic-viscoelastic finite element model of dielectric actuators*. Comput. Methods Appl. Mech. Engrg., accepted for publication, 2015.

5.2 Reviewed proceeding publications

1. T. Gail, R. Hoffmann, M. Miezal, G. Bleser, and S. Leyendecker. *Towards bridging the gap between motion capturing and biomechanical optimal control simulations*'. In Proceedings of the ECCOMAS Thematic Conference on Multibody Dynamics, 12 pages, Barcelona, Spain, 29 June - 2 July 2015.
2. M.W. Koch and S. Leyendecker. *Structure preserving optimal control of a 3d-dimensional upright gait*. In Proceedings of the ECCOMAS Thematic Conference on Multibody Dynamics, 12 pages, Barcelona, Spain, 29 June - 2 July 2015.
3. T. Gail, R. Hoffmann, M. Miezal, G. Bleser, and S. Leyendecker. *Towards bridging the gap between motion capturing and biomechanical optimal control simulations*. In Proceedings of the ECCOMAS Thematic Conference on Multibody Dynamics, 12 pages, Barcelona, Spain, 29 June - 2 July 2015.
4. H. Lang, H. Laube, and S. Leyendecker. *Various multibody dynamic models for the description of plane Kirchhoff rods*. Proceedings of the ECCOMAS Thematic Conference on Multibody Dynamics, 12 pages, Barcelona, Spain, 29 June - 2 July 2015.

5.3 Talks

1. S. Leyendecker. *A discrete variational approach to hybrid dynamical systems and optimal control*. Invited lecture, Institut für Robotik, Johannes Kepler Universität Linz, Linz, Austria, 11 February 2015.
2. S. Leyendecker. *A discrete variational approach to hybrid dynamical systems and optimal control*. Invited lecture, Department of Aerospace and Mechanical Engineering, University of Southern California, Los Angeles, California, 12 March 2015.
3. S. Leyendecker. *A discrete variational approach to hybrid dynamical systems and optimal control*. Invited lecture, Mechanics and Computation, Stanford University, Palo Alto, California, 19 March 2015.
4. D. Budday, S. Leyendecker, and H. van den Bedem. *A geometric approach to characterize rigidity in proteins*. PAMM, Vol. 15, pp. 89-90, GAMM Annual Meeting, Lecce, Italy, 23-27 March 2015.

5. M. Ringkamp, S. Ober-Blöbaum, and S. Leyendecker. *Relaxing mixed integer optimal control problems using a time transformation*. PAMM, Vol. 15, pp. 27-30, GAMM Annual Meeting, Lecce, Italy, 23-27 March 2015.
6. T. Schlögl, and S. Leyendecker. *On electrostatic-viscoelastic simulation of dielectric actuators*. PAMM, Vol. 15, pp. 421-422, GAMM Annual Meeting, Lecce, Italy, 23-27 March 2015.
7. S. Leyendecker, M. Koch, M. Ringkamp, and S. Ober-Blöbaum. *Structure preserving simulation of hybrid dynamical systems and optimal control*. 3rd German-Japanese Workshop on Computational Mechanics, Munich, Germany, 30-31 March 2015.
8. T. Schlögl, and S. Leyendecker. *Modelling and simulation of dielectric elastomer actuated multi-body systems*. EuroEAP, Poster, Tallinn, Estonia, 9-10 June, 2015.
9. D. Budday, S. Leyendecker, and H. van den Bedem. *A geometric approach to characterize rigidity of biomolecules*. EMI Conference, Stanford University, California, USA, 16-19 June 2015.
10. D. Budday, S. Leyendecker, and H. van den Bedem. *Protein conformational analysis using kinogeometric constraints*. Invited lecture, Fraser Lab at UCSF, San Francisco, California, USA, 22 June 2015.
11. H. Lang, H. Laube, and S. Leyendecker. *Various multibody dynamic models for the description of plane Kirchhoff rods*. ECCOMAS Thematic Conference on Multibody Dynamics, Barceona, Spain, 29 June - 2 July 2015.
12. M. Ringkamp, S. Ober-Blöbaum, and S. Leyendecker. *Relaxing mixed integer optimal control problems using a time transformation*. ECCOMAS Thematic Conference on Multibody Dynamics, Barceona, Spain, 29 June - 2 July 2015.
13. T. Gail, S. Leyendecker, and S. Ober-Blöbaum. *A numerical convergence study for constrained variational multirate integration*. 3rd ECCOMAS Young Investigators Conference, Aachen, Germany, 20-23 July 2015.
14. S. Leyendecker. *On the simulation and control of micro- and macroscopic motion in (electro-)mechanical systems*. Invited lecture, 7th EAM Symposium, Cluster of Excellence – Engineering of Advanced Materials, Bad Staffelstein, Germany, 23-25 November 2015.

6 Social events

Visit of the Bergkirchweih 26.05.2015



Student summer party 07.07.2015



On the Wiesent 28.08.2015



PhD defense Michael Koch 29.09.2015



Nikolaus hike 04.12.2015



Christmas party together with LTM 10.12.2015

